UNIVERSITY OF CALIFORNIA SAN DIEGO

Investigations Into Factors Regulating Early Retinal Development

A Thesis submitted in partial satisfaction of the requirements
for the degree Master of Science

in

Biology

by

Kevin W. Mazo

Committee in charge:

Professor Karl Wahlin, Chair
Professor Nicholas Spitzer, Co-Chair
Professor Michael Perry

2024

The Thesis of Kevin W. Mazo is approved, and it is acceptable in quality and form for publication on microfilm and electronically.

University of California San Diego

2024

TABLE OF CONTENTS

LIST OF FIGURES

LIST OF ABBREVIATIONS

PSC	pluripotent stem cell
SHH	sonic hedgehog
SAG	smoothened agonist
BMP	bone morphogenetic protein
ONL	outer nuclear layer
PR	photoreceptor
OPL	outer plexiform layer
HC	horizontal cell
INL	inner nuclear layer
BP	bipolar cell
IPL	inner plexiform layer
AC	amacrine cell
GCL	ganglion cell layer
M-type	midget-type
P-type	parasol-type
Ip	intrinsically photosensitive
RPC	retinal progenitor cell
CNS	central nervous system
WNT	wingless/integrated
iPSC	induced pluripotent stem cell
RNA-seq	RNA sequencing

ATAC-seq	assay for transposase accessible chromatin sequencing
rtTA	reverse tetracycline-controlled transactivator
PCA	principal component analysis
DAR	differentially accessible region
DEG	differentially expressed gene
cpm	counts per million
DAVID	Database for Annotation, Visualization and Integrated Discovery
KEGG	Kyoto Encyclopedia of Genes and Genomes
GO	Gene Ontology
UP	UniProt
HOMER	Hypergeometric Optimization of Motif EnRichment
ChIP-seq	chromatin immunoprecipitation sequencing
NPC	neural progenitor cell
dox	doxycycline
LDN	LDN-193189
RGC-iN	RGC-like induced neuron
NGF	nerve growth factor
CNTF	ciliary neurotrophic factor
NT-3	neurotrophin 3
GDNF	glial cell-line derived neurotrophic factor
sEPSC	spontaneous excitatory postsynaptic current
PIPseq	particle-templated instant partition sequencing
UMAP	uniform manifold approximation and projection

DS	directionally sensitive

ACKNOWLEDGEMENTS

I would like to acknowledge Professor Karl Wahlin for all his support for me and dedication for me, and for being such a great mentor. He helped me grow a scientist, as a leader, and most importantly as a person. For all the hours he spent helping me, the guidance he gave me, the intellectual freedom, and the fact he never gave up on me, I am truly grateful.

I would like to acknowledge Devansh Agarwal, Nathaniel Kemmerer, Manan Chopra, Shawna Jurlina, Nick Dash, Hope Do, Sonia Rivero, Sam Williams, Chris Chung, Ryan Wong, Mona Roshan, Grace Kim, Aleksandra Dragazova and all other lab members both past and present who have provided emotional and scientific support during my time working on my project.

I would like to acknowledge my friends and family for all their support and guidance that allowed me to work on my research and thesis. I am truly grateful for all the support they have provided.

Chapter 2 is based upon a previously published article that appears in *Cells* in 2022 entitled Chromatin Accessibility and Transcriptional Differences in Human Stem Cell-Derived Early-Stage Retinal Organoids. I would like to Anna Ogato for creating the cell lines used in this study. I would like to acknowledge Melissa Jones for cell line generation and organoid differentiation used for bioinformatic analysis in this study. I would like to acknowledge Devansh Agarwal, Manan Chopra, and Hope Do for participating in the bioinformatic analysis performed in this study. I would like to acknowledge my co-authors: Melissa K. Jones, Devansh Agarwal, Manan Chopra, Shawna L. Jurlina, Nicholas Dash, Qianlan Xu, Anna R. Ogata, Melissa Chow, Alex D. Hill, Netra K. Kambli, Guorong Xu, Roman Sasik, Amanda Birmingham, Kathleen M. Fisch, Robert N. Weinreb, Ray A. Enke, Dorota Skowronska-Krawczyk, and Karl J. Wahlin. The thesis author was an investigator and author of this paper.

Chapter 4 is based upon a previously published article that appears in *npj Regenerative Medicine* in 2023 entitled "Human retinal ganglion cell neurons generated by synchronous BMP inhibition and transcription factor mediated reprogramming". I would like to acknowledge Ryan Wong for creating the cell lines used in this study. I would like to acknowledge Nick Dash and Devansh Agarwal for culturing and growing the RGC-iNs analyzed in this study. I would like to acknowledge Nic Oesch for performing all electrophysiology in this study. I would like to acknowledge Devansh Agarwal, Manan Chopra, and Hope Do for participating in the bioinformatic analysis performed in this study. I would like to acknowledge my co-authors: Devansh Agarwal, Nicholas Dash, Manan Chopra, Maria P. Avila, Amit Patel, Ryan M. Wong, Cairang Jia, Hope Do, Jie Cheng, Colette Chiang, Shawna L. Jurlina, Mona Roshan, Michael W. Perry, Jong M. Rho, Risa Broyer, Cassidy D. Lee, Robert N. Weinreb, Cezar Gavrilovici, Nicholas W. Oesch, Derek S. Welsbie, and Karl J. Wahlin. The thesis author was an investigator and author of this paper.

Diagram panels in figures 1, 2, 3, and 5 were created using BioRender. Graphs in figures 3 through 16 were created using Graphpad Prism 9.

After completed drafts were written, ChatGPT was used to revise text for brevity and clarity, not for content.

VITA

2022 Bachelor of Science in Neurobiology, University of California San Diego

2024 Master of Science in Biology, University of California San Diego

PUBLICATIONS

Jones MK, Agarwal D, Mazo KW, Chopra M, Jurlina SL, Dash N, Xu Q, Ogata AR, Chow M, Hill AD, Kambli NK, Xu G, Sasik R, Birmingham A, Fisch KM, Weinreb RN, Enke RA, Skowronska-Krawczyk D, Wahlin KJ. Chromatin Accessibility and Transcriptional Differences in Human Stem Cell-Derived Early-Stage Retinal Organoids. Cells. 2022 Oct 28;11(21):3412. doi: 10.3390/cells11213412. PMID: 36359808; PMCID: PMC9657268.

Agarwal D, Do H, Mazo KW, Chopra M, Wahlin KJ. Restoring vision and rebuilding the retina by Müller glial cell reprogramming. Stem Cell Res. 2023 Feb;66:103006. doi: 10.1016/j.scr.2022.103006. Epub 2022 Dec 20. PMID: 36563542.

Agarwal D, Dash N, Mazo KW, Chopra M, Avila MP, Patel A, Wong RM, Jia C, Do H, Cheng J, Chiang C, Jurlina SL, Roshan M, Perry MW, Rho JM, Broyer R, Lee CD, Weinreb RN, Gavrilovici C, Oesch NW, Welsbie DS, Wahlin KJ. Human retinal ganglion cell neurons generated by synchronous BMP inhibition and transcription factor mediated reprogramming. NPJ Regen Med. 2023 Sep 29;8(1):55. doi: 10.1038/s41536-023-00327-x. PMID: 37773257; PMCID: PMC10541876.

Devansh Agarwal, Kevin W. Mazo, Manan Chopra, Derek Stuart Welsbie, Robert Weinreb, Ray Enke, Karl J Wahlin; Early Transcriptional Dynamics of Retinal Ganglion Cells Generated by Direct Conversion. Invest. Ophthalmol. Vis. Sci. 2023;64(8):1615.

FIELD OF STUDY

Major Field: Biology
Studies in Ophthalmology
Professor Karl Wahlin

ABSTRACT OF THE THESIS

Investigations Into Factors Regulating Early Retinal Development

by

Kevin W. Mazo

Master of Science in Biology

University of California San Diego, 2024

Professor Karl Wahlin, Chair
Professor Nicholas Spitzer, Co-Chair

Retinogenesis, the development of the retina, is regulated by dynamic changes in transcriptional expression and the chromatin landscape. While model organisms have contributed significantly to understanding retinal development, they do not allow studies of human-specific conditions. We utilized a SIX6-eGFP/VSX2-tdTomato dual fluorescent pluripotent stem-cell (PSC) line and grew retinal organoids (ROs) through 45 days. RNA- and ATAC-seq analyses through 45 days revealed transcriptomic and chromatin-landscape regulatory changes that drive retinal development and the activation of retinal specific pathways. To study an early modifier of retinal development we also investigated the Sonic Hedgehog

(Shh) signaling pathway by modulating the timing and concentration of a smoothened agonist (SAG) in SIX6-eGFP/POU4F2-tdTomato dual reporter ROs. Early SAG treatment led to the development of non-retinal tissue while later treatment favored retinal development, indicated by robust POU4F2-tdTomato expression. To investigate factors governing the formation of retinal ganglion cells (RGCs; the first cell born in the eye), we developed an inducible transgene cassette expressing the transcription factors (TFs) NEUROG2-ATOH7-ISL1-POU4F2 which, in combination with Bone Morphogenic Protein (BMP) inhibition, led to robust formation of RGC-like neurons in as little as one week. An RGC-like identity was validated via fluorescent reporter expression, transcriptomic analysis, and electrophysiology. Our findings provide a better understanding of the complex interplay of transcriptional regulation, chromatin dynamics, and microenvironmental cues in RO development and advancing our understanding of retinal biology. Generating RGC-iNs illuminates factors governing RGC formation and provides insight into the early formation of the ey

Chapter 1 INTRODUCTION

Human Retina Organization, Cell Types, and Lamination.

Vertebrate visual sensation occurs in the retina of the eye. Cells of the vertebrate retina are stratified into clearly defined layers. These layers include the outer nuclear layer (ONL) housing photoreceptors (PRs), outer plexiform layer (OPL) composed of horizontal cells (HCs), inner nuclear layer (INL) containing bipolar cells (BCs), inner plexiform layer (IPL) consisting of amacrine cells (ACs), and ganglion cell layer (GCL) populated with retinal ganglion cells (RGCs) [1] (Figure 1A). During phototransduction, photoreceptors detect photons and initiate a messaging cascade that converts photons into cyclic GMP, which ultimately works to close calcium ion channels [2]. This closure induces a hyperpolarization of PRs, leading to decreased action potential activity that signals to BCs. Thus, photoreceptors are turned off (not activated) in response to light. BCs are classified into on-bipolar cells and off-bipolar cells. Off-bipolar cells are activated by glutamate signaling, indicating a lack of photon detection in PRs, while on-bipolar cells contain an inhibitory mGluR6 glutamate receptor which inhibits action potential activity in the presence of glutamate thereby inhibiting action potential activity in the dark [3]. BPs subsequently signal to RGCs, which consist of a variety of distinct subtypes. Three RGC subtypes include midget (M-) ganglion cells, parasol (P-) ganglion cells, and intrinsically photosensitive (ip-) retinal ganglion cells, with these cell types comprising 90%, 5%, and 1% of RGCs respectively [4; 5]. Finally, the axons of RGCs then bundle together to form the optic nerve, which projects to the Lateral Geniculate Nucleus of the hypothalamus, establishing connectivity to the brain for further processing.

Transcription Factors Involved in Ventral Central Nervous System Patterning.

The transcription factors Six3 and Six6 regulate the growth of retinal progenitor cells (RPCs) as well as the hypothalamus and pituitary [6; 7]. As the retina further develops, distinct cell types are born. Around 12 weeks of human development retinal progenitor cells begin to express Atoh7 which is required for RGC formation in all vertebrates [8]. RGC formation is followed by the birth of *CRX* expressing cones, Prox1 expressing HCs, Pax6 expressing ACs, Nrl expressing rods, and Vsx2 expressing BCs [9]. While these factors are exclusive to the mature retina, RPCs express many of these cell type markers including Pax6 [10]. Many of these factors are individually expressed in a variety of tissues, such as SIX6 in both the hypothalamus and retina or POU4F2 expression in both RGCs and the cortex[11; 12]. The co-expression of SIX6 and POU4F2, however, is exclusive to the retina. This necessitates a combinatorial expression of these transcription factors for retinal development. Each of these transcription factors work to regulate signaling pathways that are important for terminal cell type differentiation [13] (Figure 1D). Pax6 expression, for example, is regulated by bone morphogenetic protein (BMP) and works to regulate Shh activity.

Ventral/Dorsal Patterning.

In early central nervous system (CNS) development, three primary brain vesicles form - the prosencephalon, mesencephalon, and rhombencephalon [14] (Figure 1B). These primary vesicles then further develop into secondary vesicles, with the prosencephalon splitting into the telencephalon and diencephalon, the mesencephalon remaining, and the rhombencephalon dividing into the metencephalon and myelencephalon. These secondary vesicles further develop into different regions in the adult brain. The telencephalon develops into the cerebrum, the diencephalon develops into the eye/thalamus/hypothalamus, the mesencephalon develops into the

midbrain, the metencephalon develops into the pons and cerebellum, and the myelencephalon develops into the medulla oblongata [15] [16] [17]. During this process, pathway patterning orchestrated by factors such as the wingless/integrated (Wnt), Shh, and BMP pathways plays a major role in distinguishing between different vesicles of the CNS and determining the specific tissue types that arise from these vesicles [13]. Within the diencephalon, these pathways distinguish between ventral and dorsal tissues, with Wnt and BMP promoting a dorsal fate and Shh promoting a ventral fate [18] (Figure 1C). Other factors work to promote dorsalization and ventralization within the eye. During the development of the retina, an asymmetric distribution of gene T-box transcription factor -2 (TBX2), -3 (TBX3), and -5 (TBX5) within the GCL coordinate to promote a dorsal retina-cell fate [19]. The ventral anterior homeobox -1 (VAX1) and -2 (VAX2) genes work in conjunction to ventralize the developing eye field and promote the formation of the optic nerve via an inhibition of the gene paired box 6 (PAX6) [20].

Retinal Organoids.

While animal models have made invaluable contributions to scientific research, there are certain research questions that animal models fail to address. Animal models fail to mimic human-specific biological processes due to genetic differences and fail to allow for precise regulation of small molecule concentrations and gradients. This underscores a need for alternative research platforms. Furthermore, stem cell-based models allow research to be performed with human cells, enabling greater manipulation and control over experimental variables. While PSC culture techniques and protocols have been used for research purposes as far back as 1981, the use of human-based stem cells has been controversial due to ethical concerns associated with harvesting embryonic stem cells [21]. With the discovery of the Yamanaka factors Oct3/4, Sox2, Klf4, and c-Myc in 2006, so-called induced pluripotent stem cells (iPSCs) could now be derived from

somatic tissues such as fibroblast or blood cells simply by the transient expression of these factors [22]. Subsequent advances in stem cell research have led to development of organoid based research models. In the eye field, human iPSC derived optic vesicles were first generated in 2009 by Meyer and colleagues, and the first retinal organoid (RO) was differentiated in 2012 by Nakano and colleagues by modulating the expression of Wnt and Shh pathways [23; 24]. Wnt activity was inhibited via the small molecule IWR-1-endo during early differentiation, and this was followed by an activation of the Shh pathway via the small molecule SAG to push organoids towards retinal formation. While RO protocols typically do not add SAG until one week of development, previous studies generating hypothalamic organoids have taken advantage of early Shh activation to do so [24; 25]. Hypothalamic organoids are generated by treating with SAG, often in combination with other Shh activators such as purmorphamine and even SHH itself, often as early as the day of differentiation [26] [27]. Temporal dynamics of SAG treatment cause major changes in the development of 3D ROs, which implies a critical window for SAG timing.

Chapter 2 GENERATION AND BIOINFORMATIC ANALYSIS OF EARLY ORGANOIDS

Generation of Human Stem Cell Derived Retinal Organoids.

Retinogenesis, the formation of the retina, involves the division and specialization of cells into a complex and multilayered structure. While the mechanisms regulating retinogenesis are not well understood, ongoing studies suggest that it is regulated by spatiotemporal changes in transcription factor and signaling pathways. Recent advancements in the use of human PSCs have allowed for novel methods to study retinogenesis in a human context. While many studies have identified transcriptomic changes in later organoids, there has been less emphasis on earlier stages of eye field development. To address this, we performed both bulk RNA-seq to identify transcription factor expression changes and ATAC-seq (Assay for Transposase-Accessible Chromatin sequencing) to identify changes in chromatin accessibility and regulatory elements of the transcriptome. Specifically, we sought to identify transcription factors expressed early in retinal development. To ensure that we were studying retinas, and no other neural cell types, we used a dual reporter PSC cell line which expressed the early eye field marker SIX6 as early as 15 days in conjunction with the expression the retinal progenitor marker VSX2 as early as day 25. To create this line, an IMR90.4 PCS line expressing eSpCas9 and rtTA at different alleles of the AAVS1 locus was used as the background for CRISPR-Cas9 based integration of a p2A-h2b-eGFP sequence at the endogenous SIX6 locus (Figure 2A) [7]. This line was hereafter referred to as SIX6-GFP. Next, a p2A-tdTomato sequence was introduced into the VSX2 locus just before the stop codon (Figure 2B). To validate these changes, we grew organoids as described in the methods section through day 50, imaged for fluorescent expression of SIX6-GFP and VSX2-tdTomato

(Figure 2C-L), and performed both bulk RNA-seq and ATAC-seq at five-day intervals from days 0-25 as well as day 35 and day 45 [25] [28].

Transcriptomic Sequencing of Early Eye Field Development.

To identify transcriptomic changes that occur in early retinal development, we analyzed bulk RNA and ATAC-seq datasets described above. For RNAseq transcript, raw reads were trimmed with TrimGalore and quality assessed with FastQC. Transcripts were aligned to the reference hg38 human genome using HISAT2[29]. HISAT2 outputs were fed into featureCounts for transcript quantification [30]. Subsequently, the count tables were input into the DESeq2 statistical package for determination of differential transcript expression between samples [31]. For ATAC-seq, peak calling, peak height measurements and motif analyses were done using a sliding window of 400 bp in HOMER [32]. Alignment of ATAC-seq peaks with the hg38 human genome revealed distinct patterns (Figure 3A). Principal component analysis (PCA) of both the RNA-seq and ATAC-seq of organoids from days 0-25 showed a clear temporal trajectory of both RNA expression and epigenetic accessibility. Notably, tight clusters were observed among replicates at each time point (Figure 3B). We found that chromatin accessibility peaks were mostly localized within intergenic sites (44.16%), introns (39.61%), and promoters (10.08%), and there were relatively fewer peaks found within exons (2.511%), transcriptional termination sites (1.29%), 3'-UTRs (1.06%), non-coding sequences (0.82%), and 5'-UTRs (0.47%) (Figure 3C). We verified SIX6 and VSX2 expression by fluorescence microscopy and analyzed changes in chromatin accessibility mRNA transcript expression by ATAC-seq and RNA-seq respectively. While *SIX6* had accessible chromatin peaks at its promoter from days 5-25, *VSX2* did not have any accessible peaks through day 25 (Figure 3D). This is consistent with RNA-seq data, which confirmed SIX6 expression beginning at day 5 through day 25. VSX2 expression, however, did

not onset by day 25 suggesting that there was a decoupling between chromatin accessibility and mRNA expression.

To gain additional insight into unknown patterns of gene expression, we next sought to identify new differentially accessible regions (DARs) and differentially expressed genes (DEGs). Comparative analyses of ATACseq and RNAseq datasets between day 25 and day 0 revealed 2138 differentially accessible peaks (|logFC|>0.58, p-value<0.050) and 1333 differentially expressed genes (|logFC|>0.58, FDR<0.05) with 326 of these in common (Figure 3E). Genes that were both differentially accessible and differentially expressed between days 0 and 25 notably included many known biologically relevant transcription factors and signaling pathways. For example, *DLX5*, which is a key component of the BMP signaling pathway, was differentially accessible and differentially expressed between days 0 and 25 [33]. *DLX5* increased from day 0 to day 25 from 0 counts per million (cpm) to 25.75cpm (Log2FC=26.75). This was accompanied by an increase in motif enrichment, with an increase from FC=1.15 to FC=1.39 in the number of target sequences containing the DLX5 motif compared to those containing background motifs (Figure 3F).

Pathway Analysis of Early Eye Field Development.

Common DAR/DEGs were used to perform pathway analysis using DAVID (The Database for Annotation, Visualization and Integrated Discovery) [34]. DAVID identified 1487 pathways from KEGG (Kyoto Encyclopedia of Genes and Genomes) pathways, Gene Ontology (GO) terms, and Uniprot (UP) keywords, of which 68s pathways were statistically significant (FDR<0.1) (Figure 4A) [35] [36] [37] [38]. Notably, several significant pathways included the biologically relevant pathways of regulation of axonogenesis (-log10FDR=9.98), negative regulation of mitotic cell cycle (-log10FDR=6.34), and dendrite development (-log10FDR=5.42). As organoids develop, they undergo a loss of pluripotency and transition to a post-mitotic state. This is evidenced

by a decrease in the expression of pluripotency markers such as *OCT4*, *THY1*, and *EPCAM* between days 0-25 combined with an increase in the expression of neural progenitor markers such as *HES5*, *SIX3*, and *NCAM1* (Figure 4B) [39] [40]. Further significant pathways were nervous system development (-log10FDR=6.59), axonogenesis (-log10FDR=1.48), and axon guidance (-log10FDR=2.92). This underscores ongoing retinal differentiation characterized by the upregulation of pathways that promote crucial steps of axon and neuron maturation that are necessary for retinal maturation [41]. The downregulation of pluripotency genes, in combination with the upregulation of axon guidance genes, indicates a shift away from pluripotency towards a retinal specific fate.

Motif Discovery and Analysis.

HOMER was used to perform peak calling and motif discovery on peak tag directories at each timepoint to characterize and elucidate relevant transcription factor and gene motifs within the chromatin landscape [32]. At early timepoints such as days 0 and 5, we found that pluripotency related motifs such as OCT4-SOX2-TCF-NANOG were highly enriched, which coincided with a decrease in peak heights at pluripotency factor transcriptional start site accessibility. At later timepoints we found that while pluripotency factors such as *POU5F1*, *TCCF7*, and *NANOG* had decreased chromatin accessibility and motifs for retinal transcription factors such as NeuroD1 and NeuroG2 were more highly enriched. This corresponded to an increase in the accessibility peak heights of these retinal transcription factors (Figures 4C-D). The concurrent decrease in expression and accessibility of pluripotency factors in combination with an increase in expression and accessibility of retinal transcription factors, upregulation of neurogenic pathways, and changes in motifs during retinal development suggests that chromatin accessibility and transcriptional regulation play important roles in governing retinal development.

Discussion.

The use of organoid protocols that combine a SIX-eGFP reporter with a VSX2-tdTomato reporter allow for studies of retinal development at the earliest stages of pluripotency and onset of retinogenesis. We were able to perform bioinformatic analyses of early developing retinal organoids (ROs) and identified pathways such as pluripotency and Wnt signaling that participate in early retinal development. Organoid variability within and between experiments, however, remains an obstacle to studies designed to use PSC based models to recapitulate human retinal development and diseases. Some studies attribute variability as intrinsic to cell lines [42; 43], while others attribute it to differences in differentiation itself [44; 45]. Our approach using dual stage-specific reporters allows us to mitigate variability by selecting only for organoids expressing both reporters, thus ensuring a retinal phenotype. Furthermore, the dual approach of RNA- and ATAC-seq enables a complementary gene regularity study that elucidates the nature of these gene regulatory interactions. While the abundance of peak accessibility and gene transcripts of *SIX6* at early stages is concordant with the observed eGFP fluorescence, the low levels of *VSX2* accessibility peaks and transcripts at day 25 is contradictory to the observed tdTomato expression. While this is surprising, previous studies have identified a disconnect between gene expression and chromatin accessibility, with studies even suggesting that the chromatin accessibility profile of the retina does not necessarily match the cell-type abundance of the retina[46; 47].

Further motif analysis performed using HOMER highlighted that chromatin accessibility alone does not imply high gene expression. While a few genes such as *NEUROG2* and *NEUROG1* had significantly positive correlations between chromatin accessibility and gene expression, many others did not. Interestingly, *TCF4* had a strong negative correlation between accessibility peaks and transcripts, implying that transcription factors may be binding to the *TCF4* promoter and

preventing its transcription. While the parallel use of both ATAC- and RNA-seq helps reveal functionally relevant chromatin landscape changes, there is some ambiguity left in this analysis. Our study does not allow cell type specific investigations that are difficult to identify with bulk sequencing. A combination of single cell/nuclear RNA sequencing with single cell ATAC sequencing can be performed in the future to reveal cell type specific gene regulation, chromatin accessibility, and cell heterogeneity. Future studies can combine chromatin immunoprecipitation sequencing (ChIP-seq) assays to further experimentally validate the role of specific transcription factor motifs that drive retinogenesis.

Pathway analysis of developing organoids highlights the role of developmental pathways in retinogenesis. Pathways for neuron development involving axonogenesis, dendrite genesis, and decrease of pluripotency are found to be relevant during organoid growth. The prevalence of these neuron-specific pathways underscores the importance of neuron formation and neuron maturation in retinal development. A downregulation of pluripotency pathways in combination with an upregulation of neuronal pathways indicates that a shift away from pluripotency and towards neurons plays a critical role in retinogenesis.

Acknowledgement.

Chapter 2 is based upon a previously published article that appears in Cells in 2022 entitled Chromatin Accessibility and Transcriptional Differences in Human Stem Cell-Derived Early-Stage Retinal Organoids. I would like to Anna Ogato for creating the cell lines used in this study. I would like to acknowledge Melissa Jones for cell line generation and organoid differentiation used for bioinformatic analysis in this study. I would like to acknowledge Devansh Agarwal, Manan Chopra, and Hope Do for participating in the bioinformatic analysis performed in this study. I would like to acknowledge my co-authors: Melissa K. Jones, Devansh Agarwal, Manan

Chopra, Shawna L. Jurlina, Nicholas Dash, Qianlan Xu, Anna R. Ogata, Melissa Chow, Alex D. Hill, Netra K. Kambli, Guorong Xu, Roman Sasik, Amanda Birmingham, Kathleen M. Fisch, Robert N. Weinreb, Ray A. Enke, Dorota Skowronska-Krawczyk, and Karl J. Wahlin. The thesis author was an investigator and author of this paper.

Chapter 3 THE ROLE OF SONIC HEDGEHOG SIGNALING IN EARLY RETINAL DEVELOPMENT

Retinal Embryogenesis.

During embryogenesis and further retinal formation, regulation in the expression of morphogens and growth factors orchestrates the differentiation of human pluripotent stem cells (hPSCs) into various tissue and cell types. Embryogenesis begins with the development of three germ layer tissues (endoderm, mesoderm, and ectoderm) which give further rise to the entire organism. The ectoderm undergoes additional specialization into the central nervous system (CNS), giving rise to the three primary vesicles of CNS development: the prosencephalon, mesencephalon, and telencephalon. The prosencephalon undergoes a secondary division into the secondary vesicles of the telencephalon and diencephalon. The diencephalon in turn gives rise to the eye, thalamus, and hypothalamus. Morphogen, growth factor, and signaling molecule regulation works to determine the terminal fate of PSCs during differentiation.

Sonic Hedgehog Orchestration of Retinal Development.

Sonic Hedgehog (SHH) signaling plays a critical role in determining the fate of PSCs during CNS development [48]. The SHH pathway is highly tuned *in vivo* and promotes a ventral fate in developing systems. The earliest protocols used to generate human-derived ROs relied on an activation of the SHH pathway with the small molecule Smoothened Agonist (SAG) in combination with an inhibition of the Wingless/Integrated (WNT) pathway [24]. The timing of SAG treatment is important for proper development in the context of ROs protocols. Protocols for generating hypothalamic organoids require a treatment with SHH activators during the early stages of differentiation, often as early as the first day of differentiation [27]. The significant impact of

small temporal changes in SAG treatment induction suggested a critical window for SAG treatment that determines the fate of 3D ROs.

The Role of SAG Timing in Retinal Organoid Development.

To investigate the impact of SAG timing on cell fate we grew ROs while beginning SAG treatment at various timepoints in the span of initial eye field formation. We found that organoids that were not treated with SAG had dim levels of SIX6-eGFP fluorescence at 15 days, but this fluorescence did not sustain through 45 days (Fig. 5A-C) indicating a non-retinal phenotype. Treatment of SAG beginning at early timepoints (days 1-6) which is then sustained through 15 days of differentiation led to an early and bright expression of SIX6-eGFP at day 15 (Fig. 5D-E). Despite sustained SIX6 expression through day 45, POU4F2-tdTomato expression was absent suggesting differentiation into SIX6-expressing non-retinal cells (Fig. 5F). Organoids treated with SAG beginning at intermediate timepoints (days 7-10) sustained through 15 days had dim SIX6-eGFP fluorescence at 15 days (Fig. 5G-H), with increased fluorescent intensity at 45 days combined which with an expression of POU4F2-tdTomato fluorescent reporter expression indicates a retinal lineage (Fig.5I). Organoids treated with SAG beginning at a later timepoint (days 11-14) sustained through 15 days had dim SIX6-eGFP fluorescence at day 15 (Fig. 5J-K), which somewhat sustained expression through 45 days and was extended to a subsequent development of dim POU4F2-tdTomato fluorescence (Fig. 5L). This suggests a development of ROs that is less robust than intermediate SAG treatment. Quantitative analysis of GFP intensity was performed using an ImageXpress Micro Confocal High-Content Imaging System (Molecular Devices) for image acquisition and the MetaXpress software package with a custom module to segment and mask GFP + areas. We measured the GFP fluorescent intensity in arbitrary units of each organoid and found that organoids treated with SAG at earlier timepoints tended to have

greater a slightly greater average, minimum, and maximum GFP fluorescent intensity than any other treatment group (Fig. 5M-P). Organoids treated at intermediate and later timepoints had similar average, minimum, and maximum GFP intensity to the control organoids. Increased fluorescent reporter expression of SIX6-eGFP suggests that while all ROs express SIX6, the expression of SIX6 does not conclusively indicate a retinal identity.

The Role of SAG21k Timing in Retinal Organoid Development.

To investigate the differences between cell fate in response to SAG21k treatment timing we grew ROs with SAG21K treatment intervals beginning at various timepoints in the span of early to late eye field formation. We found that organoids that were not treated with any SAG21k had no expression of SIX6-eGFP fluorescence at timepoint from 15 days through 45 days (Fig. 6A-C) indicating a non-retinal phenotype. Organoids treated with SAG21k beginning at either an early (beginning at days 1-6) or intermediate (beginning at days 7-10) sustained through 15 days of differentiation had an early and bright expression of our SIX6-eGFP reporter at day 15 which was sustained through 45 days (Fig. 6D-I) despite an absence of POU4F2-tdTomato expression. This indicated a non-retinal phenotype. The limited red fluorescent expression that appeared by day 45 did not appear to be confined to any cells, but rather appears to be diffusely expressed and indicative of necrotic tissue. Organoids treated with SAG21k beginning at a later timepoint (days 11-14) sustained through 15 days had some dim SIX6-eGFP fluorescence at day 15 which diminished through 45 days, which when coupled with diffuse POU4F2-tdTomato fluorescence at day 45 is suggestive of necrotic tissue (Fig. 6J-L). Quantitative analysis of GFP intensity was performed using an ImageXpress Micro Confocal High-Content Imaging System (Molecular Devices) for image acquisition and the MetaXpress software package with a custom module to segment and mask GFP + areas. We measured the GFP fluorescence of each organoid in arbitrary

unit and found that organoids treated with SAG21k at earlier and intermediate timepoints had a greater average, minimum, and maximum GFP fluorescent intensity when compared to other treatment groups (Fig. 6M-P). Organoids treated at any later timepoints had similar average, minimum, and maximum GFP intensities as the control organoids However, this was often due to from autofluorescence resulting from cell death. The failure of any organoids to develop convincing POU4F2-tdTomato expression indicates that treatment with 100nM SAG21k prevents organoids from developing into a retinal fate.

Intermediate Organoid Treatment with SAG Concentration Gradients.

We treated organoids with varying concentrations of SAG from days 8 through 15 to investigate the impact that different levels of SHH signaling have on organoids at an intermediate timepoint. While untreated ROs failed to develop any SIX6-eGFP or POU4F2-tdTomato fluorescence at any timepoint (Fig. 7A-B), organoids treated with any concentration of SAG between 9.4nM and 1200nM developed SIX-eGFP fluorescence by day 15 that was sustained through 45 days (Fig. 7C-H). All organoids treated with 9.4-1200nM SAG from days 8 through 15 further developed POU4F2-tdTomato fluorescence, indicating a retinal phenotype. Organoids treated with higher concentrations of SAG (2400-4800nM) initially developed SIX-eGFP fluorescence by day 15, but this expression did not sustain through 45 days. The organoids further failed to develop POU4F2-tdTomato fluorescence (Fig. 14G-H). The lack of POU4F2-tdTomato fluorescence suggests that they have a non-retinal phenotype. Quantitative image analysis of GFP fluorescence using an ImageXpress Micro Confocal High-Content Imaging System (Molecular Devices) for image acquisition and the MetaXpress software package (Fig. 7Q-S) validated the observed trends regarding the impact of SAG concentration on organoids.

Intermediate Organoid Treatment with SAG21k Concentration Gradients.

We treated organoids with varying concentrations of SAG21k from days 8 through 15 to investigate the impact that different levels of SHH signaling have on organoids at an intermediate timepoint. While untreated organoids failed to develop any SIX6-eGFP or POU4F2-tdTomato fluorescence at any timepoint (Fig. 7I-J), organoids treated with any concentration of SAG between 3.1nM and 800nM developed SIX-eGFP fluorescence by day 15 (Fig. 7K-P). Quantitative image analysis of GFP fluorescence using an ImageXpress Micro Confocal High-Content Imaging System (Molecular Devices) for image acquisition and the MetaXpress software package (Fig. 7W-Y) validated the observed trends regarding the impact of SAG concentration on organoids.

Elucidation of the Role of Sonic Hedgehog Signaling in Organoid Development.

The profound influence that SAG and SAG21k treatment had on the GFP intensity of ROs indicates a key role that SHH signaling plays during retinal development. The observed morphological differences between early treated and later treated organoids suggests that there is an important timing window for SHH signaling which determines the neural tissue that develops. Early induction of SHH signaling in combination with inhibition of WNT signaling primes organoids to develop into hypothalamus [49]. Delaying SAG treatment, however, enabled a shift to a retinal fate. This shift suggests that the timing of hedgehog signaling is critically important. Furthermore, modulations in the levels of SAG exposure of organoids changes the type of tissue that develops, which mimics the importance of SHH gradients that *in vivo* change which type of tissue develops [50].

One limitation of our study was the growth of multiple optic vesicles in one organoid. Our RO protocol leads each organoid to grow multiple vesicles which can grow subsequently into a variety of tissues including retina, hypothalamus, and cortex. Each of these tissues secrete factors which often inhibit the growth of other tissue types. Manual excision of optic vesicles to reduce

the mass of growing organoids is typically performed between 10-15 days, with each optic vesicle being isolated and grown separately. Organoids that fail to develop fluorescent reporter expression are further segregated and discarded to prevent the secretion of factors that inhibit retinal growth. This allows for a more controlled analysis of individual tissue types and their respective developmental trajectories. Our study, however, did not excise optic vesicles due to issues of scalability. In order to screen such a large range of temporal and concentration conditions, organoids were grown at an extremely high throughput in terms that rendered optic vesicle excision highly impractical, It is worth noting that there are RO generating protocols which do not require optic vesicle excision [51]. In hindsight, these protocols may have offered technical advantages by reducing variability. Unknown factor secretions may be interacting with the retinal tissues in complex ways which can mask the precise impact that changes in SAG treatment have on RO growth and differentiation. Furthermore, non-retinal vesicles on an organoid may be secreting factors that promote the growth off non-retinal tissue. This would mean that our study into the role of SAG signaling may be investigating the role of SHH signaling on non-retinal tissues. Another challenge with our study is the inherent variability associated with organoid culture. Organoids are notorious for their complexity and variability which can affect experimental outcomes. To mitigate issues of variability, we grew multiple biological replicates that successfully developed dual fluorescent reporter expression (n=3). While we were able to successfully grow multiple replicates that expressed both SIX6-eGFP and POU4F2-tdTomato, a substantial number of additional replicates failed to exhibit any retinal-specific fluorescent reporter expression. The observed variability between differentiations highlights the inherent challenges in organoid research and suggests a need for protocol standardization and optimization to increase

experimental reproducibility and reliability. This standardization may include investing other factors known to be involved in retinal development such as BMP signaling.

Despite flaws in our study, it does shed light on the role of SHH signaling in retinal development. While we elucidate the role of SHH signaling in the retina, we acknowledge that we failed to explore the influence of other morphogens that have been previously implicated in retinal differentiation protocols. We did not investigate the role of BMP signaling, for example, which is used *in vivo* to promote a dorsal fate and has recently been used in protocols to promote a dorsal retinal differentiation [51]. Future investigations could use concentration gradients of SAG and BMP7 to create a more physiological retinal differentiation protocol. Techniques such as 3D bioprinting and factor-soaked alginate beads offer promising avenues for the generation of SAG and BMP7 gradients that would offer precise environmental control over organoid development. Culturing organoids with these more physiological morphogen gradients would allow a generation of more specific ROs that have an either ventral or dorsal morphology.

Chapter 4 GENERATION OF INDUCED RETINAL GANGLION-LIKE CELLS

Generation of Human Stem Cell Derived Induced Retinal Ganglion Cells.

A permanent death and loss of retinal ganglion cells (RGCs) characterize many irreversible causes of blindness. Strategies such as cell transplantation and endogenous regeneration offer promising possibilities for treating blindness yet require a complete understanding of the developmental program used for RGC differentiation and maturation. While these programs remain elusive, they likely require precise orchestration of developmental transcription factors. Early in eye development, morphogens and transcription factors such as Lhx2, Pax6, and Six6 work to coordinate early eye field and forebrain development [52]. At later stages of development, a different network of transcription factors including Neurogenin-2 (Neurog2), Atonal homolog-7 (Atoh7), Islet-1 (Isl1), and POU class 4 homeobox 2 (Pou4f2) work to guide neural progenitor cells (NPCs) towards a RGC-specific state [53]. Neurog2 drives neurogenesis and cell type specification, while Atoh7 primes the induction of immature RGCs. Atoh7 then stimulates the expression of downstream transcription factors Isl1 and Pou4f2, culminating in RGC maturation. In mice, Isl1 and Pou4f2 expression disruptions during development leads to errors in axon pathfinding and causes inadequate optic nerve development [34].

Existing protocols for generating human PSC-derived RGCs are slow and require immunopanning to obtain high purity [54]. To enhance and expedite the creation of enriched RGC populations, we engineered hPSCs with doxycycline (dox) inducible transgene cassettes containing *NEUROG2*, *ATOH7*, *ISL1*, and *POU4F2* either individually or in combination and integrated the cassettes into the CLYBL safe harbor (Figure 8A). We found that a synergistic approach of pre-patterning with the BMP blocking small molecule LDN-193189 (LDN) in combination with the overexpression of *NEUROG2*, *ATOH7*, *ISL1*, and *POU4F2* generates RGC-

like induced-neurons (RGC-iNs) with long, branched neurites and POU4F2-tdRomato reporter expression in 94% of cells. Validation of RGC-like identity was further corroborated by transcriptional profiles as determined by RNA-seq and single-cell RNA-seq (scRNA-seq) as well as electrophysiological studies.

Direct Conversion of RGC-iNs via NEUROG2, ATOH7, ISL1, and POU4F2 overexpression.

To explore the contributions of NEUROG2, ATOH7, ISL1, and POU4F2 in RGC development and maturation we generated a polycistronic cassette that uses a dox-inducible promoter coupled (TetO) coupled to *NEUROG2*, *ATOH7*, *ISL1*, and *POU4F2* (NAIP2) and transfected it into POU4F2-p2A-tdTomato cells. While untreated control cells had PSC-like morphology, dox treated transiently transfected cells had limited populations of neurons among PSC-like cells (Figures 8A-B). Encouraged by the partial conversion of transiently transfected cells into neurons, we then stably integrated the NAIP2 cassette into the CLYBL safe harbor using a high-fidelity EnCas12a (Figure 8C). We then selected for stably integrated cells by using zeocin resistance and found that NAIP2 integrated cells treated with 1.0µg/mL dox and 100nM LDN developed long branched neurites by day 6 while treated control cells did not. Furthermore, among all transcription factor combinations tested, only *NEUROG2* and NAIP2 produced high levels of neurons (Figures 8D-L). Interestingly, only NAIP2 cells expressed the POU4F2-tdTomato RGC reporter (Figure 8M). NAIP2 cells generated dual TUJ+/POU4F2+ cells at conversion efficiencies of 88%, 94%, and 90% in IMR90.4, GM23720 and WA09 PSCs respectively. While multiple transcription factor combinations can efficiently generate neurons, only the NAIP2 combination is able to generate POU4F2+ RGC-like cells.

RNA-seq Analysis of RGC-iNs.

We performed RNA-seq on PSCs (n=3) and dox-treated controls (CTL, n=5), *NEUROG2* expressing cells (n=4), *NEUROG2* and *ATOH7* expressing cells (NA, n=4), and NAIP2 expressing cells (n=4) to identify the transcriptional identity of our induced-neurons. Principal component analysis (PCA) from DESeq2 showed consistent clustering of biological replicates for each condition, with separate clusters delineated for PSCs, controls, and induced neurons. Within the induced-neuron cluster, *NEUROG2*, NA, and NAIP2 groups exhibited distinct separation from each other (Figure 9A). This was further confirmed by visualization of the expression of the top 500 most highly expressed genes in the NAIP2 group across all treatment groups (Figure 9B). While pan-neuronal markers such as *RBFOX3*, *TUBB3*, *SYT1*, and *DLG4* were detected in all induced neuron groups (i.e. *NEUROG2*, *NA*, *NAIP2*), RGC specific markers such as *POU4F1*, *POU6F2*, and *NRN1* were much more highly upregulated in the NAIP2 treatment group than in any other induced-neuron group (Figures 9C-D).

Pathway Analysis of RGC-iNs.

When we performed pathway analysis on NAIP2 treated cells using RNA-seq data, we found an enrichment of pathways that are biologically relevant for neurons. Among these pathways were calcium signaling pathway, neuroactive ligand-receptor, ion channel, and cAMP/MAPK signaling (Figure 10A). RNA-seq data depicted an active process of axonogenesis and axon outgrowth that occurs during RGC development. Many genes involved in RGC axonogenesis such as *ISLR2* and *ELAVL3* were expressed in NAIP2 cells but not found in PSCs, CTLs, or other non-RGC neurons (Figure 10B). RGC-iNs expressed functional guidance cues that steer axons either towards or away from specific molecular signals. While some ephrin ligands, which are involved in cell-to-cell communication, are expressed in both neuronal and non-neuronal populations (e.g.,, *EFNB1*, *EFNB2*, *EPHA2*), others like *EFNA3*, *EFNB3*, *EPHA5*, and *EPHB2* were upregulated in

our neuronal populations and with an increased expression in RGC-iNs at week 4 compared to week 1 (Figures 10B-C). Signaling factors known to mediate RGC axonogenesis were further regulated over time. The RGC axon guidance receptors *ROBO2* and *ROBO3* were expressed at 1 week of development and decreased in expression over time. Interestingly, their ligands *SLIT1* and *SLIT2* increased in expression through week 4 (Figure 10D). The class 3/4/6 inhibitory axon-guidance semaphorin proteins and their plexin family receptors regulate optic chiasm decussation during RGC axon finding. We found that semaphorins and plexins increased in expression from week 1 through week 4 (Figures 10E-G) [55]. Interestingly, the class 6 semaphorin gene *SEMA6A* was expressed in the non-neuronal PSCs and CTLs, but not in RGC-iNs. This, however, is consistent with previous reports [56].

Temporal Analysis of RGC-iNs.

We performed RNA-seq on NAIP2 cells (n=4) through 4 weeks and CTLs (n=4) through 3 weeks to evaluate temporal transcriptomic changes occurring in RGC formation. Comparing RGC-iNs with CTLs revealed a diverging trajectory over time (Figure 11A). We looked at the expression profiles of different retinal cell type markers to validate an RGC-like phenotype in NAIP2. We found that while RGC-iNs express pan-neuronal markers (e.g., *SYN1*, *DLG4*, and *RBFFOX3*) and RGC markers (e.g., *POU4F1*, *POU4F2*, *SNCG*), they do not express any photoreceptor (e.g.,, *RHO*, *CRX*, *ARR3*, *LHX4*), bipolar cell (e.g.,, *NETO1*, *VSX2*, *OTX2*), amacrine cell (e.g., *GAD1*, *TFAP2B*, *TFAP2C*), horizontal cell (e.g., *LHX1*, *CALB1*, *PTF1A*), or glial markers (e.g., *S100B*, *OLIG2*, *GLAST*, *GFAP*) (Figure 11B). RGC-iNs expressed excitatory and inhibitory neuron markers, further suggesting an RGC-like transcriptome. Analysis of the expression of individual NAIP2 factors showed that while *NEUROG2*, *ATOH7*, and *ISL1* all peaked in expression at one week when dox treatment is stopped, *POU4F2* expression peaked at

four weeks (Figure 11C). Notably, although the NAIP2 factors decreased in expression after one week, their expression was still maintained. NAIP2 expression was sustained through three weeks, and even increases at week four. The same trend was observed with neurotrophic receptors, which play a vital role in neural and neuroprotective function [57]. Neurotrophic receptors including the nerve growth factor (NGF) receptor *NGFR*, and the ciliary neurotrophic factor (CNTF) receptor *CNTFR* are expressed at one week and then decrease in expression through week three followed. This is followed by a peak in expression at week four. Other neurotrophic receptors such as the NGF receptor *NTRK1* (TrkA), the neurotrophin-3 (NT-3) receptor *NTRK3* (TrkC), and the glial cell line-derived neurotrophic factor (GDNF) receptor *GFRA1* all peaked in expression at one week and decreased in expression through four weeks. Interestingly, the Brain Derived Neurotophic Factor (BDNF) receptor *NTRK2* (TrkB) increased in expression over the course of 4 weeks (Figure 11D). It is possible, however, the reason that *NTRK2* was the only neurotrophic receptor to increase over time is due to a positive selection of *NTRK2* in response to BDNF treatment through four weeks. RGC-iNs further expressed genes involved in packing, docking, release, and reuptake of neurotransmitters that enable action potential.

Electrophysiological Activity of RGC-iNs.

After looking at neurotrophic receptor expression, we then looked for the expression of ion channels in RGC-iNs to indicate their capability for electrophysiological activity. We found that our RGC-iNs express a variety of ion channels responsible for electrophysiological activity in neurons (Figure 12A). We detected voltage-gated sodium (e.g., *SCN2A*/Nav1.3a, *SCN3B*/Bav1.3b, *SCN9A*/Nav1.7) and potassium channels (*KCNA2*/Kv1.2, *KCNA3*/Kv1.3, *KCNA6*/Kv1.6, *KCNC4*/Kv3.4, *KCND1*/Kv4.1, *KCND4*/Kv4.3) which modulate and regulate the amplitude and duration of action potential trains. To assess the electrophysiological function of RGC-iNs, we

performed current clamp and whole-cell voltage clamp recordings at two weeks and four weeks. Current clamp recordings showed that RGC-iNs were capable of firing repeated action potentials, while voltage-lamp recordings revealed sodium and potassium currents that were characteristic of RGCs with increasing maturity from two weeks to four weeks (Figures 12B-C). To investigate the presence of functional glutamate receptors, we transiently applied puffs of AMPA. We observed that AMPA treatment caused large inward currents with a reversal potential of 0mV on a linear I-V trace (Figure 12D), This is consistent with the functional activation of GluA2 receptors [58]. We also observed spontaneous excitatory post-synaptic currents (sEPSCs) which indicates the potential for RGC-iNs to form synapses (Figure 12E). These sEPSCs displayed fast kinetics that were blocked by the AMPA antagonist DNQX, which is consistent with AMPA-mediated synaptic events[59].

Single Cell Sequencing of RGC-iNs.

We performed particle-templated instant partition sequencing (PIP-seq) of RGC-iNs at 7, 14, and 21 days to identify any subtype specific diversity that may exist in RGC-iN populations [60]. For day 7 (n=3) we obtained 3,440 cells (31,880 median transcripts/cell), for day 14 (n=2) we obtained 1,665 cells (39,208 median transcripts/cell), and for day 21 (n=3) we obtained 2,380 cells (31,880 median transcripts/cell). Cells from each timepoint were clustered using the Louvain algorithm and projected onto 2D space by UMAP (uniform manifold approximation and projection) to visualize cell clusters and marker gene expression (Figure 13A). While RGC-iNs had sustained expression of pan-neuronal markers (e.g., *TUBB3*, *MAP2*, *SYT1*) and RGC specific markers (e.g., *STMN2*, *GAP43*, *SNCG*), there was no discernible expression of cell type specific markers for other retinal cell types (e.g., photoreceptors, bipolar cells, amacrine cells, horizontal cells, and glia) (Figures 13B-C). We compared RGC-iN scRNA-seq at two weeks data to publicly

available human retinal scRNA-seq datasets (including 45 day old retinal organoids (ROs), 59 day old fetal RGCs, and 40 day old iPSC-derived RGCs) and found that RGC-iNs integrated well within each of these data sets [61; 62; 63] (Figure 13D). Analysis showed that RGC-iNs express subtype specific markers for both alpha- (e.g., *SPP1*, *PIGO*, *RPP14*) and directionally sensitive (DS)- (e.g., *DCX*, *CDH6*, *JAM2*) subtype RGCs (Figure 13E). These subtype specific markers, however, were distributed across many clusters. The murky distribution of alpha- and DS- subtype specific markers across clusters suggests that it may be difficult to resolve functional classifications of human RGCs based upon sequencing data alone. We took a previously annotated human scRNA-seq dataset, extracted the top 2000 highly variable genes at day 21 of our dataset, and used a machine learning based predictive label transfer model to explore whether other morphology based classification systems may be better suited for categorizing RGC-iNs, [5; 64]. While the human adult retina contains 90% midget (M)-type RGCs, 5% parasol (P)-type RGCs, 1% intrinsically photosensitive (ip) RGCs, and 4% undefined RGC subtypes, we found that RGC-iNs were composed of 40% M-type, 13% P-type, 7% ipRGC, and 40% undefined RGC subtypes (Figure 13F). While the predictive label transfer found that 7% of RGC-iNs were ipRGCs, we did not find any expression of the ipRGC marker *OPN4* in our dataset, suggesting that the label transfer approach may be labelling RGC subtypes based upon subtle gene expression profile differences and may over- or underestimate the actual number of each RGC subtype.

Discussion.

We created enriched RGC-like cell populations by recapitulating developmental cues that guide RGC formation. We created a transgenic overexpression cassette to express four RGC specific transcription factors (NEUROG2, ATOH7, ISL1, POU4F2) which when combined with small molecule inhibition of BMP generated neurons that mimic RGCs in transcriptomic and

electrophysiological profiles. Cell replacement and neuroprotective therapeutics necessitate fine control over cell-type reprogramming for the generation of human cell-type specific models. Recent studies have generated several types of neurons by reprogramming with transcription factors, microRNAs, and small molecule treatment including a study which combined dual small molecule-based SMAD inhibition with *NEUROG2* overexpression to generate forebrain neurons [65] [66]. Neurog2 mutant mice have shown reduced neurogenesis and RGC formation, while ectopic expression of *Isl1* and *Pou4f2* promote RGC formation [67; 68]. Overexpression of *ATOH7* in differentiating organoids has been shown to enhance RGC formation in early optic vesicles, and overexpression of *NEUROG2* and *ATOH7* in differentiating organoids has been shown to increase the number of POU4F2, NF145, and RBPMS positive RGCs [27; 69]. While each of these studies overexpressed transcription factors, they each only overexpressed one transcription factor at a time. We used concurrent overexpression of 4 transcription factors and found a significant enhancement in POU4F2-tdTomato+ signals when compared to the overexpression of any individual transcription factor alone. Our protocol generated RGC-like neurons in as little as 5 days, which is remarkably faster than the typical take 3-4 weeks required to generate RGC-iNs at a much lower efficiency [54; 70; 71]. It is worth noting, however, that our protocol does investigate all transcription factors implicated in RGC development. It is possible that other transcription factor combinations may be more effective for reprogramming RGCs. Future therapeutic approaches utilizing endogenous regeneration may need to explore other transcription factor combinations to maximize conversion efficiency.

While molecular signatures have been used to identify more than 30 RGC subtypes in mice, it is believed that there is less RGC subtype diversity in humans [62; 72] [73]. Functional classifications in humans have identified alpha-, DS-, and ip- RGC subtypes, and

morphological/projection classifications have identified M-type, P-type, and ipRGC subtypes. While adult RGCs can be classified into alpha-, DS-, and ipRGCs based on molecular markers, RGC-iNs are much more difficult to classify as subtype specific marker expression is spread across most cell clusters identified via scRNA-seq. The same is true of RGC-iNs classifications into M-type, P-type, and ipRGCs. This may be due to an immaturity of RGC-iNs. RGC-iNs may need further time or environmental cues to mature and fully develop into distinct RGC subtypes. Furthermore, it may be possible that a more exact transcription factor composition is necessary to generate specific RGC subtypes. This would prevent the formation of RGC subtypes using the NAIP2 transgene cassette under any conditions. Overall, direct programming studies offer a promising approach to the generation of human RGC-like neurons that can be used for developmental studies, neuroprotective studies, and cell transplantation studies. Our approach can be adapted to use other transcription factor combinations to generate a wide variety of neuronal populations.

Acknowledgement.

Chapter 4 is based upon a previously published article that appears in *npj Regenerative Medicine* in 2023 entitled "Human retinal ganglion cell neurons generated by synchronous BMP inhibition and transcription factor mediated reprogramming". I would like to acknowledge Ryan Wong for creating the cell lines used in this study. I would like to acknowledge Nick Dash and Devansh Agarwal for culturing and growing the RGC-iNs analyzed in this study. I would like to acknowledge Nic Oesch for performing all electrophysiology in this study. I would like to acknowledge Devansh Agarwal, Manan Chopra, and Hope Do for participating in the bioinformatic analysis performed in this study. I would like to acknowledge my co-authors: Devansh Agarwal, Nicholas Dash, Manan Chopra, Maria P. Avila, Amit Patel, Ryan M. Wong,

Cairang Jia, Hope Do, Jie Cheng, Colette Chiang, Shawna L. Jurlina, Mona Roshan, Michael W. Perry, Jong M. Rho, Risa Broyer, Cassidy D. Lee, Robert N. Weinreb, Cezar Gavrilovici, Nicholas W. Oesch, Derek S. Welsbie, and Karl J. Wahlin. The thesis author was an investigator and author of this paper.

Chapter 5 MATERIALS AND METHODS

Cells.

IMR90.4 iPSCs and WA09 ES (both from WiCell) and EP1.1 cell (Donald Zack; JHU) were used for the following study. Cells were routinely tested for mycoplasma by PCR. PSCs were used with approval from the UC San Diego Institutional Review Board. Single-cell passage and maintenance of PSCs. Stem cells were maintained antibiotic free on 1% (vol/vol) Matrigel (MG)-GFRTM (#354230; BD Biosciences) extracellular matrix (ECM) coated dishes at 37°C under hypoxic conditions (10% CO2/5%O2) in mTeSR1 (Stem Cell Technologies) as previously described [74] [68] [75] [76]. Cells were passaged every 4-6 days, with Accutase (#A6964; Sigma) for 10-12 minutes, dissociated into single cells, quenched with mTeSR1 plus 5μM blebbistatin (B; #B0560; Sigma), pelleted at 80 x g for 5 minutes, resuspended in mTeSR1+B and plated at 2,000 cells per single well of a 12-well plate. After 48 hours, cells were fed with mTeSR alone.

Plasmid preparation for transfection.

For routine growth of plasmids, we used chemically competent Stable E. coli cells (#C3040I; NEB). DNA for transfection was prepared using the endotoxin-free grade Plasmid Plus Maxi Kit (#12963; Qiagen) or ZymoPURE Plasmid Midiprep Kits (#11-550; Zymo). Purified plasmid was resolved by agarose gel electrophoresis to rule out RNA or genomic DNA contamination. Plasmids used for quantitative studies of HDR efficiency were never thawed more than 3 times to prevent unwanted degradation of plasmids. PureLink RNA Mini Kit (#12183020; Thermo Fisher Scientific) was used to purify total RNA to be used for subsequent cDNA synthesis.

Constructs for generating Tet-inducible HF-iCas9 Cells.

The laboratory previously created inducible Cas9 PSCs to facilitate gene-editing. The method is briefly described here. To create HF-ieCas9 cells we targeted the AAVS1 safe harbor site inserting a reverse tetracycline-controlled trans-activator (rtTA) expression cassette at one allele and a 3G-TET regulated eSpCas9 at the other. When bound to doxycycline, constitutively expressed rtTA binds to the Tet operator and ieCas9 expression is induced. The rtTA coding sequence was provided by AAVS1-Neo-M2-rtTA plasmid (Addgene; #60843) whereas the ieSpCas9 coding sequence was amplified from eSpCas9(1.1)(Addgene #71814) [77] and cloned into the AAVS1-puro-Cas9 donor (Addgene #58409) . Briefly, the AAVS1 donor shell was amplified with Phusion Polymerase (#F548L; Invitrogen) using the oligos Cas9backbone_F and Rev and the ieSpCas9 insert was amplified using the oligos Cas9insert_for and Cas9insert_rev (Table 1). PCR products were cleaned using DNA Clean and Concentrator-5 columns (#D4014; Zymo Research) and donor and insert PCR products were fused together using Gibson assembly reagents (#E2611S; NEB), followed by overnight digestion with Dpn1 enzyme (#R0176L; NEB) to remove parental template DNA. The Gibson product was transformed into chemically competent Stable E. coli cells and colonies were miniprepped and verified by Sanger sequencing. For the AAaVS1 targeting, phosphorylated an oligo duplex of the AAVS1_esp_T1 forward and reverse oligos were ligated into BbsI cut pSpCas9(BB)-2A-puro (PX459) V2.0 backbone (Addgene #62988) using Quick ligase (NEB according to the manufacturer's specifications).

Reporter cells as a backbone.

The cell line background used for this study was previously made by other lab members. Briefly a SIX6-p2a-eGFP IMR90 iPSC line was made using the following approach. The SIX6 gene was targeted by amplifying a 1,311 base pair donor fragment (657 left homology arm and 654 base right homology arm). Immediately before the SIX6 stop site, a p2a- H2B-eGFP cassette was inserted in-frame. A similar approach was taken to generate a BRN3B-p2a-tdTomato reporter. Both donors were electroporated into stem cells and stably integrated into the genome via CRISPR-Cas9 gene editing.

Sequencing Directed Differentiation.

Optic vesicles were generated as previously described [25] with minor modifications. Cell culture medium used for differentiation was as follows: BE6.2-NIM (B27 + E6 at 2X concentration) (neural induction medium) consists of DMEM (#11965; Invitrogen) supplemented with 1% B27 vitamin A (-) (#12587010; Invitrogen) and 2X E6 supplement (38.8 mg/L insulin (#11376497001; Roche), +128mg/L L-ascorbic acid (#A8960; Sigma), 28µg/L selenium (#S5261; Sigma), 21.4 mg/L transferrin (#T0665; Sigma) and 38.8 mg/L NaHCO3). LTR (Long-Term Retina) medium was a 3:1 mix of DMEM:F12 (#11965, #11765; Invitrogen) supplemented with 1% B27 (#17504044; Invitrogen), 10% heat inactivated qualified- grade FBS (#16140071; Invitrogen), 1mM pyruvate (#11360; Invitrogen), 1xNEAA (#11140; Invitrogen), 1xGlutamax (#35050061; Invitrogen) and 1mM taurine (#T-8691; Sigma). For optic vesicle induction, PSCs maintained in mTeSR1 were used to initiate serum-free embryoid body forced aggregates. Stem cells were passaged with a longer Accutase incubation for 12 minutes and 1,000 cells in 50µl of mTeSR1+B were seeded per well into polystyrene 96-well U-bottom plates (#650180; Greiner). Aggregates were transitioned to BE6.2 medium by adding 50µl+2% MG on day 1 and 1% MG

each day thereafter. On days 4-8, a 50% medium exchange (100 µl) was performed daily and every other day thereafter. Medium contained 1% (v/v) MG and 3µM of IWR- 1e (a WNT inhibitor and AXIN2 stabilizer; #681669; EMD Millipore) from days 1-6. To increase survival and differentiation, 500nM all-trans retinoic acid (ATRA; #R2625; Sigma) was added to LTR medium from day 20. Organoids were transferred at day 10 to 15ml conical tubes, rinsed 3 times in DMEM, and resuspended in either BE6.2, BE6.2+300nM Smoothened agonist (SAG; #566660; EMD Millipore), or BE6.2+100nM Smoothened Agonist 21K (SAG21K; #5282; Tocris) with 4-6 organoids per well of a 6-well suspension plate (#657185; Greiner Bio). On day 14, organoids were fed with LTR, LTR+SAG, or SAG21K. On day 15, organoids were fed with LTR which they were maintained in for the remainder of the experiment. SAG and SAG21K were first added at the designated timepoint for experiments on SAG temporal treatment.

SAG and SAG21k Treatment Variations.

For SAG timing experiments, organoids were differentiated by adding either SAG or SAG21k at varying timepoints. SAG and SAG21k were added at beginning each timepoint from day 1 through day 14. After initially adding SAG/SAG21K, it was continually added through day 14 after which it was removed. To investigate the role of SAG treatment on organoid development, SAG and SAG21k were added to organoids either beginning at day 4 or day 8 and were continued through day 14. SAG was added at the following concentrations: 0nM, 9.4nM, 18.8nM, 37.5nM, 75nM, 150nM, 300nM, 600nM, 1200nM, 2400nM, and 4800nM. SAG21K was added at the following concentrations: 0nM, 3.1nM, 6.3nM, 12.5nM, 25nM, 50nM, 100nM, 200nM, 400nM, 800nM, or 1600nM.

Imaging and fluorescence intensity calculation.

For analysis, GFP fluorescence arbitrary units (gfp a.u.) were used to reflect the mean total intensity per object. In later studies we used an ImageXpress Micro Confocal High-Content Imaging System (Molecular Devices) for image acquisition and the MetaXpress software package with a custom module to segment and mask GFP + areas, allowing us to measure the intensity per unit area. Briefly, brightfield images were inverted and a Gaussian Filter was applied. Objects that had approximate diameter between 87.9µm and 306µm were identified and were masked. FITC channel images were then analyzed for GFP fluorescence over the masks, including average area, average GFP intensity, total integrated GFP intensity, GFP intensity standard deviation, minimum intensity, and maximum intensity. Samples were further inspected in the Cy5 channel to rule out autofluorescence or bleed through. To ensure proper masking, individuals who did not contribute otherwise to this project were asked to look at the masks applied to the retinal organoids (ROs) and determine which organoids had proper masking. Only these were used in further analysis. Quantitative measurements for brightness and intensity were imported into Prism GraphPad and plotted as line graphs.

RNA QC, library prep, and HiSeq sequencing.

Sample QC, RNA library preparations and sequencing reactions were conducted at GENEWIZ, LLC. (South Plainfield, NJ). The concentration of RNA was quantified using a Qubit Fluorometer (Life Technologies, Carlsbad, CA) and RNA integrity was assayed using a TapeStation (Agilent Technologies, Palo Alto, CA). Samples passing initial QC were prepared for sequencing using a SMART-Seq v4 Ultra Low Input Kit for full-length cDNA synthesis and amplification (Clontech, Mountain View, CA), and an Illumina Nextera XT library (Illumina, San Diego, CA) was used for sequencing library preparations. Briefly, cDNA was fragmented, and an adaptor was added using transposase, followed by limited-cycle PCR to enrich and add index to

the cDNA fragments. The final library was assessed with an Agilent TapeStation. Sequencing libraries for the 28 cDNA samples were multiplexed and sequenced using the Illumina HiSeq sequencing platform. 56 PE FASTQ files received back from Genewiz were analyzed using a customized bioinformatics workflow.

Bioinformatic analysis.

Transcript alignment of each sample was achieved using HISAT2 with the reference hg38 human genome[29]. HISAT2 outputs were fed into featureCounts for transcript quantification[30]. Subsequently, the count tables or matrices were input into the DESeq2 statistical package for determination of differential transcript expression between samples[31]. DESeq2 is available as an R package and was used to generate a principal component analysis (PCA) plot demonstrating the variance between distinct sample groups as well as similarity within sample replicates for all samples as well as the sample-to-sample distance heatmap showcasing large sample distances between various time points and tight clustering within the same replicates of a particular time point. Volcano plots were generated in RStudio using the ggplot2 package.

For ATAC-seq, peak calling, peak height measurements and motif analyses were done using a sliding window of 400 bp in HOMER (Hypergeometric Optimization of Motif EnRichment) [32]. Normalization and differential analysis (DA) were done in R using limma [78]. Principal component, hierarchical cluster analyses and scatterplots were designed using BioVinci v1.0.0 (BioTuring, Inc., San Diego, CA, USA), ATAC-seq peaks were visualized with IGViewer v2.5.3 [79], statistical analyses were completed in Galaxy/Cistrome [80] and figures were generated in Prism (v5.01; GraphPad Software, San Diego, USA). Pathway analysis was performed using DAVID (v6.8) [81] and significance was accepted at FDR < 0.1 for analysis of DEG/DARs and an FDR < 0.001 for analysis of DEGs only.

Generating diagrams.

All diagrams were generated using BioRender.

FIGURES

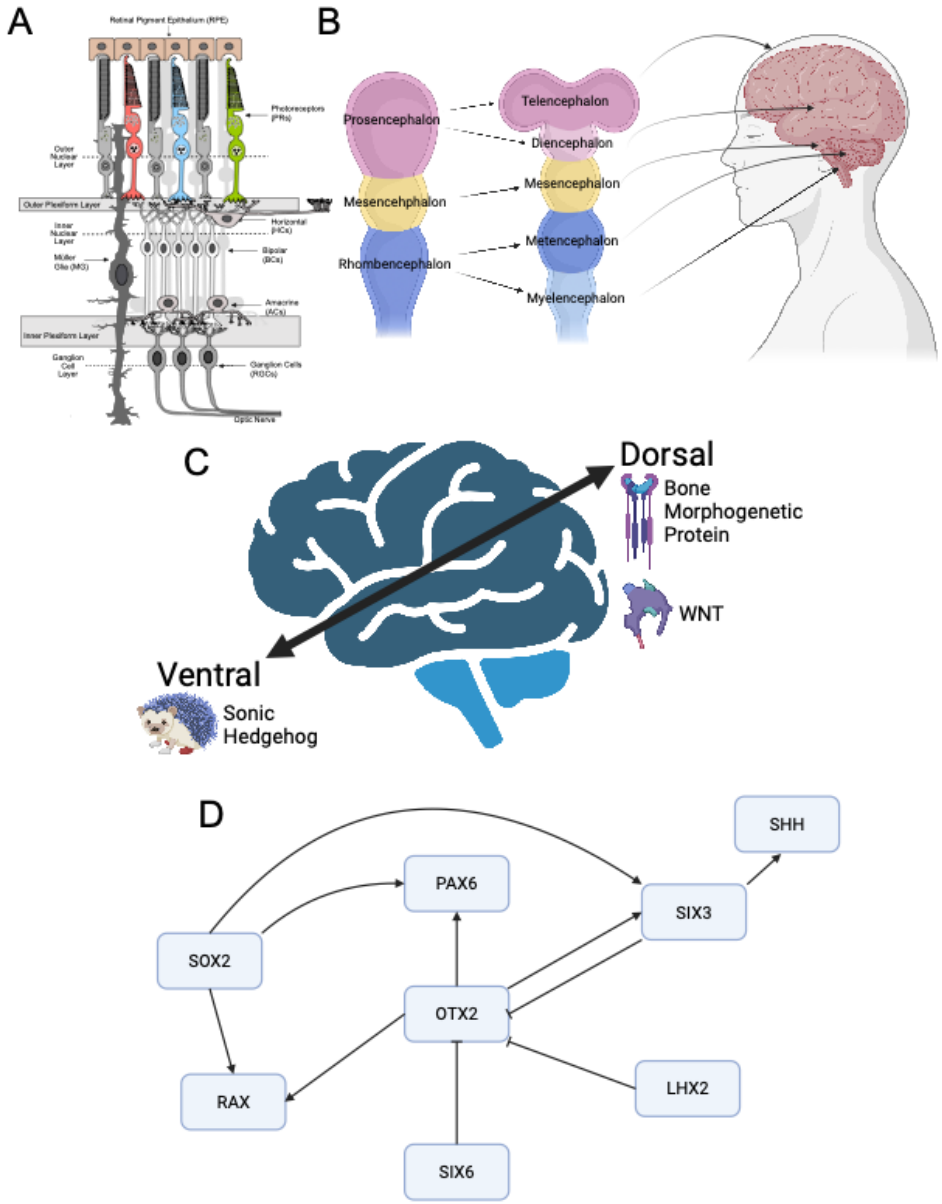

Figure 1. Pathways relevant to retinal differentiation.

(**A**) Diagram depicting the human retina including relevant cell types and layers. (**B**) Diagram depicting the development of the human central nervous system including the primary vesicles (left), secondary vesicles (center) and mature structures they develop into (right). Arrows indicate developmental trajectory. (**C**) A diagram of the brain including anatomical directions for dorsal and ventral directions. Ventralizing factors include Sonic Hedgehog Signaling, and dorsalizing factors include Bone Morphogenetic Protein signaling and WNT signaling. (**D**) A diagram depicting transcription factors that are relevant to early retinal development. Arrows indicate activation, and blunt head arrows indicate inhibition.

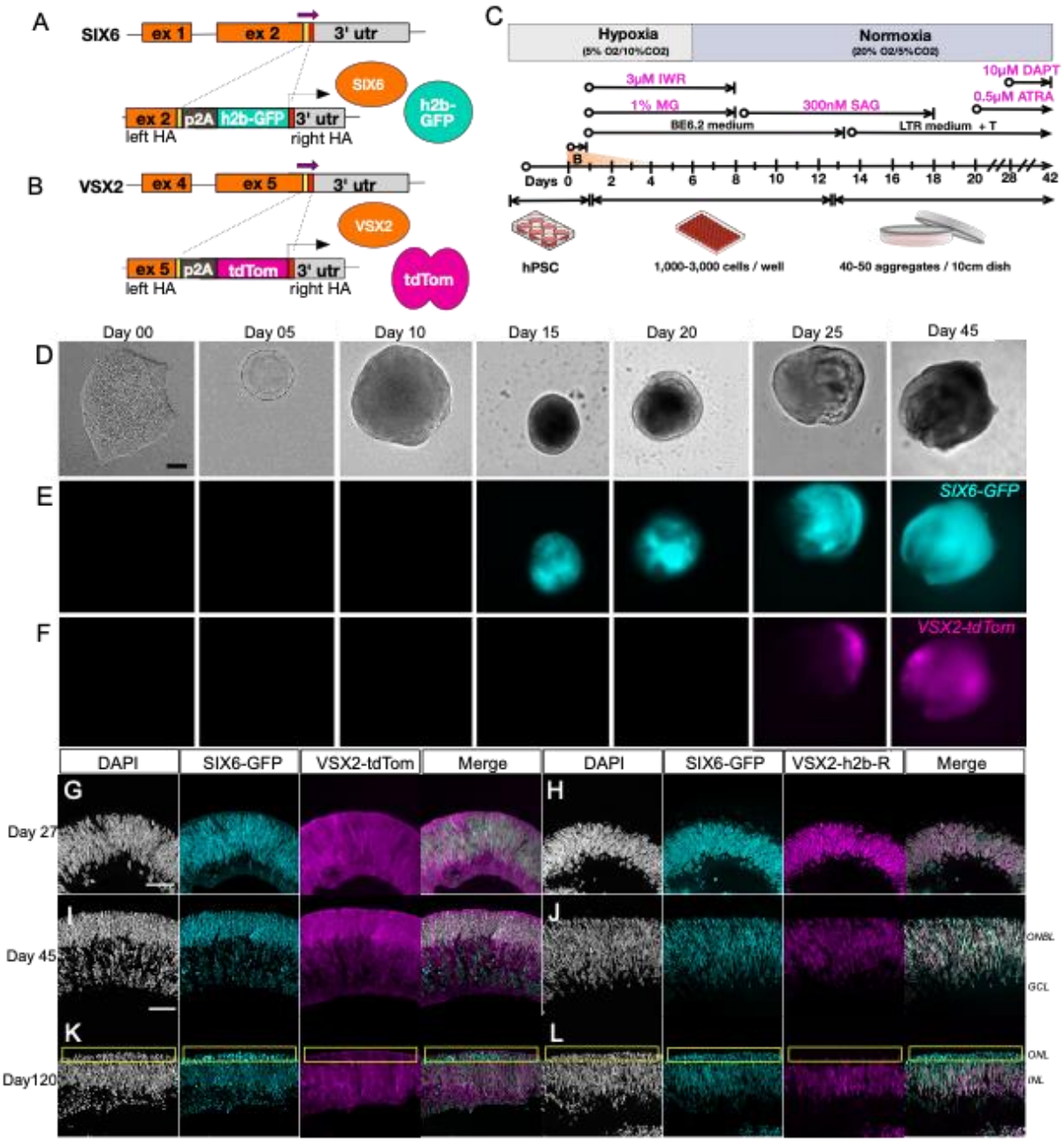

Figure 2. Generation of retinal organoids.

Taken from Jones et al., 2022. (**A**) A PSC line with a single *SIX6*-h2b-GFP reporter was (**B**) further modified with a *VSX2*-p2A-tdTomato reporter cassette. (**C**) Graphical protocol for differentiation of retinal organoids adapted from Wahlin et al., 2017. Representative images for differentiating *SIX6*-GFP/*VSX2*-tdTomato PSCs organoids in brightfield (**D**) and (**E**-**F**) *SIX6*-GFP and *VSX2*-tdTomato fluorescence visualized up to differentiation day 45. Organoids at day 15 are smaller than at day 10 due to manual cutting on day 10. Images are separate organoids and are not tracked over time. (**G**–**L**) Cross-sections of organoids from day 27 (**G**-**H**), day 45 (**I**-**J**), and day 120 (**K**-**L**) show nuclear GFP expression throughout the organoid and tdTomato expression becoming restricted over time. Panels (**G**,**I**,**K**) represent cytoplasmic *VSX2*-tdTomato reporter expression, while panels (**H**,**J**,**L**) represent nuclear *VSX2*-mRuby3. A yellow box (**K**,**L**) indicates the outer nuclear layer. Scale bars (**D**–**F**) = 100 µm; *VSX2*-tdTom = *VSX2*-tdTomato, *VSX2*-h2b-R = *VSX2*-h2b-mRuby3; Scale bar (**G**–**L**) = 50 µm.

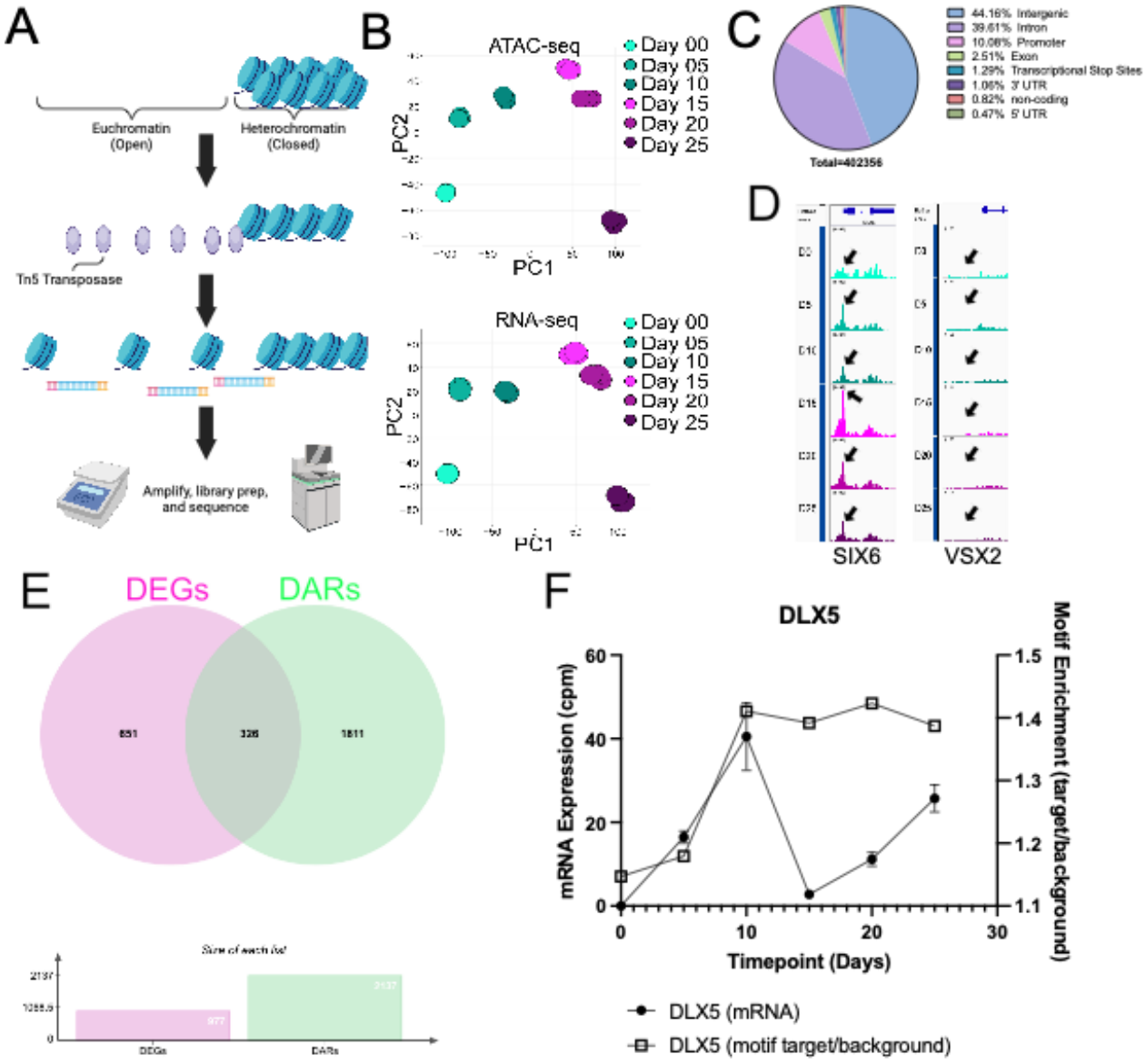

Figure 3. Trends in chromatin accessibility and gene expression.

Adapted from Jones et al., 2022. (A) A schematic diagram of the ATAC-seq workflow depicting the isolation and amplification of accessible euchromatin in preparation for next generation sequencing. (B) Principal component analysis (PCA) of ATAC-seq samples based on 62,201 peaks show a developmental progression over time with little variability between replicates (top). PCA of RNA-seq samples from days 00 through 25 based on 12,512 expressed genes show a developmental progression over time with little variability between replicates (bottom). (C) A pie chart of global genomic annotations of chromatin accessibility peaks from ATAC-seq from days 00 through 25 shows that most accessible peaks are found within intergenic and intronic genomic loci. (D) Chromatin accessibility tracks of SIX6 ATAC-seq from days 00 through 25 (left) show that while the chromatin accessibility of SIX6 at the transcriptional start site (arrow) is low at early timepoints such as days 00 and 05, the accessibility increases at later timepoints such as days 35 and 45. ATAC-seq of VSX2 gene from days 00 through 25 (right), however, shows very little chromatin accessibility at any timepoint at the transcriptional start site (arrows). (E) A Venn diagram indicating the number of Differentially expressed genes (DEGs), Differentially Accessible Regions (DARs), and the overlap of common DEG/DARs between days 0 and 25. (F) A line graph depicting the transcriptomic expression of DLX5 in counts per million (circle, left y-axis) and the chromatin accessibility of DLX5 in motif enrichment above background (square, right y-axis) over time.

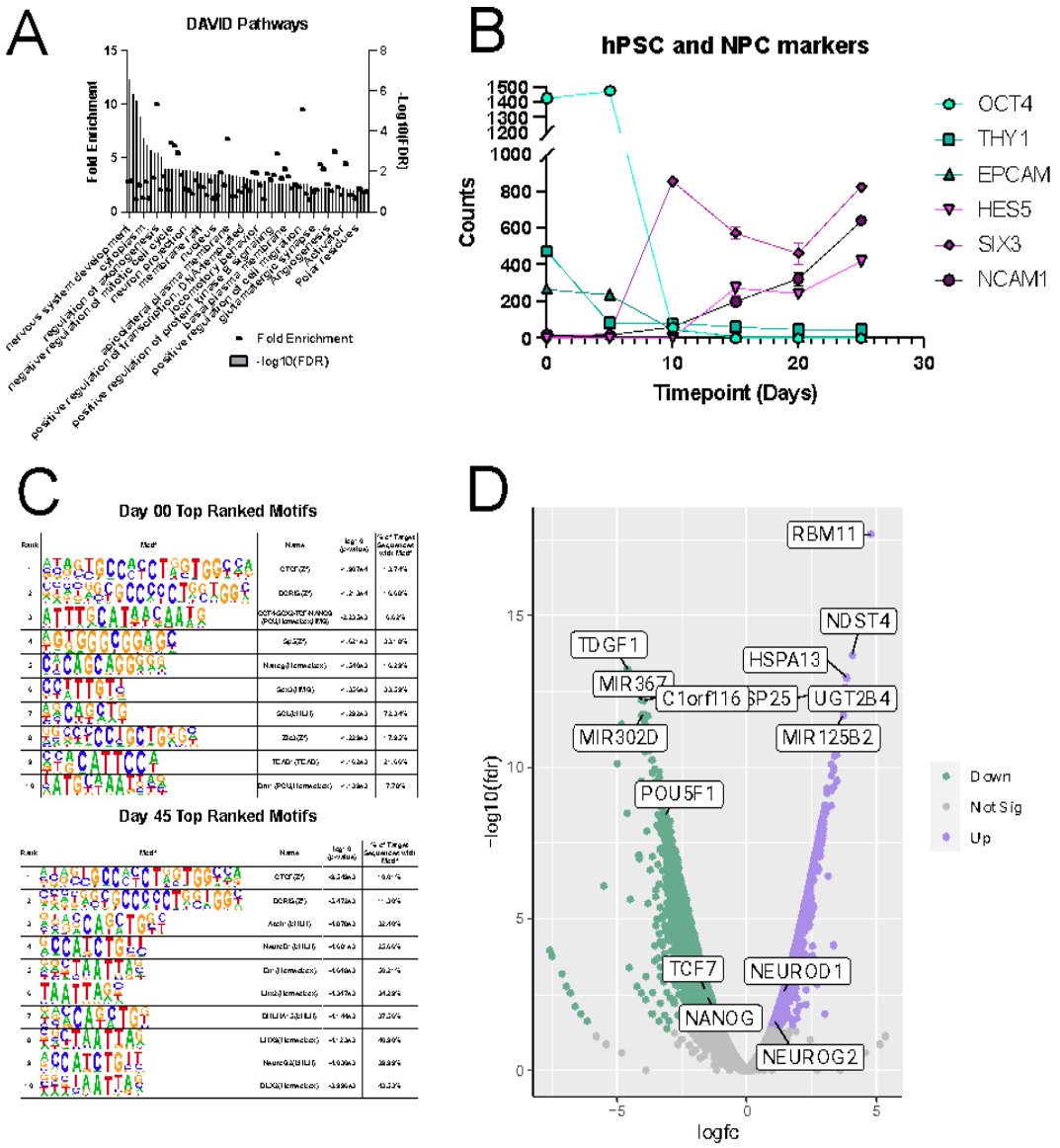

Figure 4. A shift from pluripotency to neural progenitor during early eye field formation.

Adapted from Jones et al., 2022. (**A**) Pathway analysis of combined DEG/DARs from early retinal organoids. Pathways are graphed while showing the fold enrichment of DEG/DARs in the pathway (dots, left y-axis) as well as the -log10(FDR) of the pathway (bars, right y-axis). (**B**) A line graph depicting the RNA-seq expression of select hPSC markers (green) and NPC markers (magenta). Error bars depict standard error of the mean. (**C**) Tables displaying the top 10 motifs each for Day 00 (top) and Day 45 (bottom), along with their motif name and type and the percentage of target sequences that contained the motif. Motifs were ranked according to −log10(p-values). (**D**) A volcano plot depicting the log2(FC) of chromatin accessibility peaks (x-axis) compared to the -log10(FDR) (y-axis). Statistically significant DARs are defined as having an |log2(FC)|>0.58 and an FDR<0.05. DARs that have an increase in accessibility from day 00 to day 25 are purple, while DARs that have a decrease in accessibility from day 00 to day 25 are green. Regions that are not statistically significantly differentially accessible are gray. The top 10 DARs based on FDR are labelled, as well as select DARs.

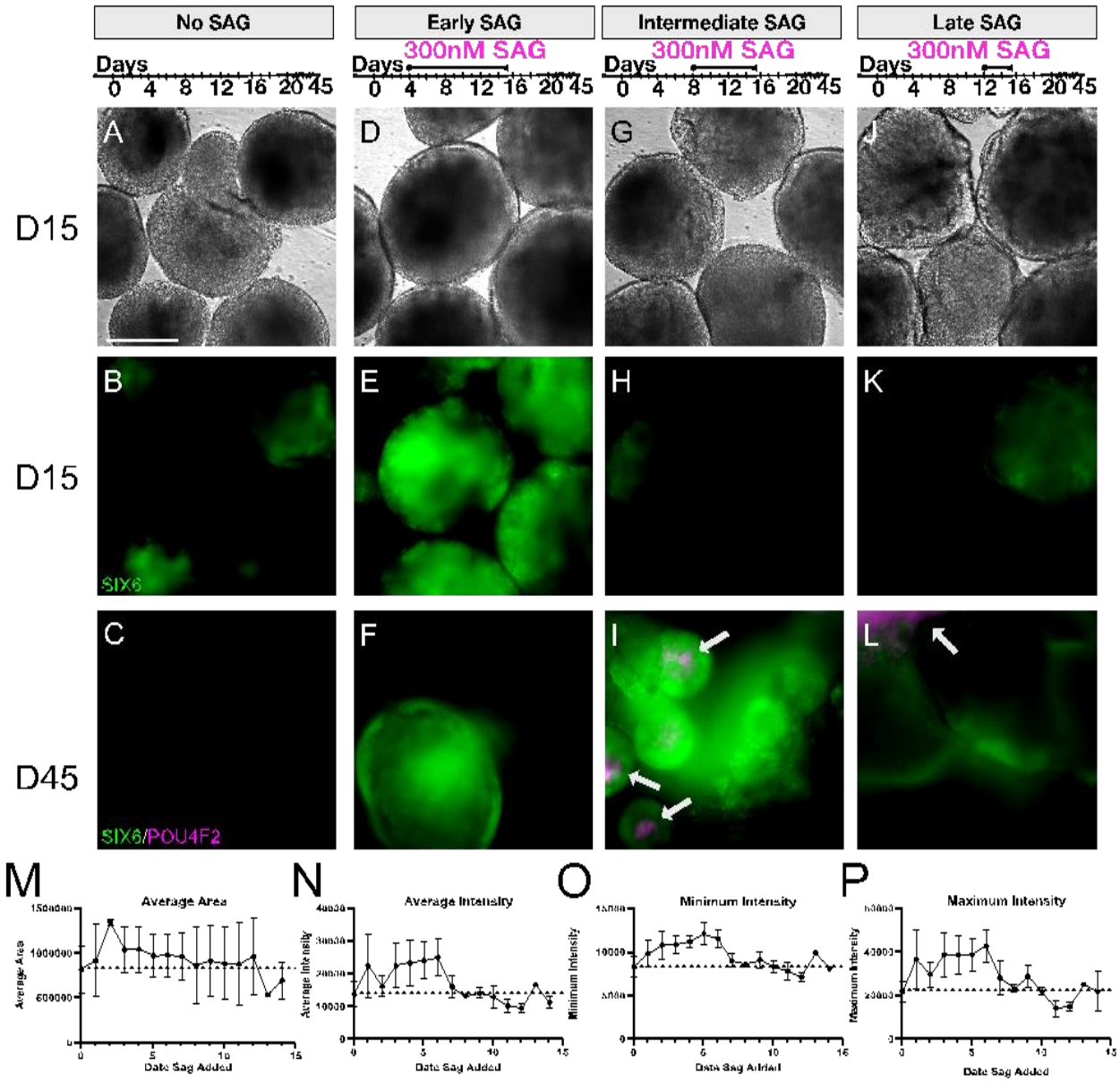

Figure 5. Identifying windows of competence for SHH induction of SIX6-eGFP and POU4F2-tdTomato using the smoothened agonist SAG.

(**A-C**) Organoids that were not treated with SAG imaged at (**A-B**) 15 days (**C**) and 45 days for GFP fluorescence. (**D-F**) Organoids treated with 300nM SAG from days 4-14 imaged at (**D-E**) 15 days and (**F**) 45 days. (**G-I**) Organoids treated with 300nM SAG from days 8-14 imaged at (**G-H**) 15 days and (**I**) 45 days. (**J-L**) Organoids treated with 300nM SAG from days 12-14 imaged at (**J-K**)15 days and (**J-K**) 45 days. (**M-P**) A graph depicting the (**M**) average area (in pixels squared), (**N**) average intensity (in arbitrary units), (**O**) minimum intensity (in arbitrary units), and (**P**) maximum intensity (in arbitrary units) of organoids treated with 300nM SAG beginning at any timepoint and all ending at 15 days. Timepoint labelled as added at day 0 are untreated organoids. Arrows label dual-fluorescence. Timepoint labelled as added at day 0 are untreated organoids. (**A-L**) scale bar represents 200µm. (**M-P**) Error bars represent standard error of the mean. Graphs above panels depict the developmental protocol used to generate the images below.

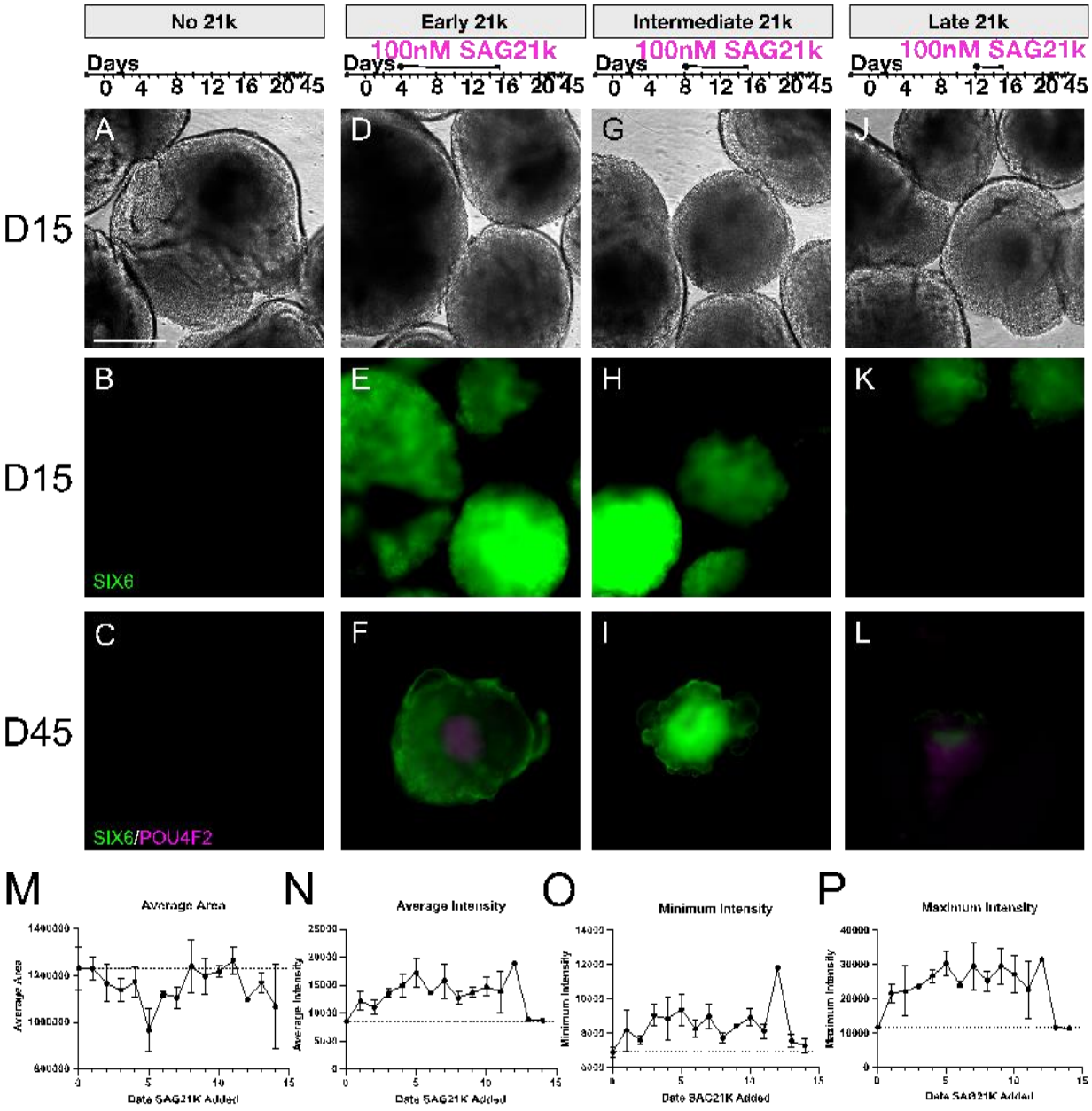

Figure 6. Identifying windows of competence for SHH induction of SIX6-eGFP and POU4F2-tdTomato using a high potency smoothened agonist SAG21k.

(**A-C**) Organoids that were not treated with SAG21k imaged at (**A-B**) 15 days (**C**) and 45 days. (**D-F**) Organoids treated with 100nM SAG21k from days 4-14 imaged at (**D-E**) 15 days and (**F**) 45 days. (**G-I**) Organoids treated with 100nM SAG21k from days 8-14 imaged at (**G-H**) 15 days and (**I**) 45 days. (**J-L**) Organoids treated with 100nM SAG21k from days 12-14 imaged at (**J-K**)15 days and (**J-K**) 45 days. (**M-P**) A graph depicting the (**M**) average area (in pixels squared), (**N**) average intensity (in arbitrary units), (**O**) minimum intensity (in arbitrary units), and (**P**) maximum intensity (in arbitrary units) of organoids treated with 100nM SAG21k beginning at any timepoint and all ending at 15 days. Timepoint labelled as added at day 0 are untreated organoids. Timepoint labelled as added at day 0 are untreated organoids. (**A-L**) scale bar represents 200µm. (**M-P**) Error bars represent standard error of the mean. Graphs above panels depict the developmental protocol used to generate the images below.

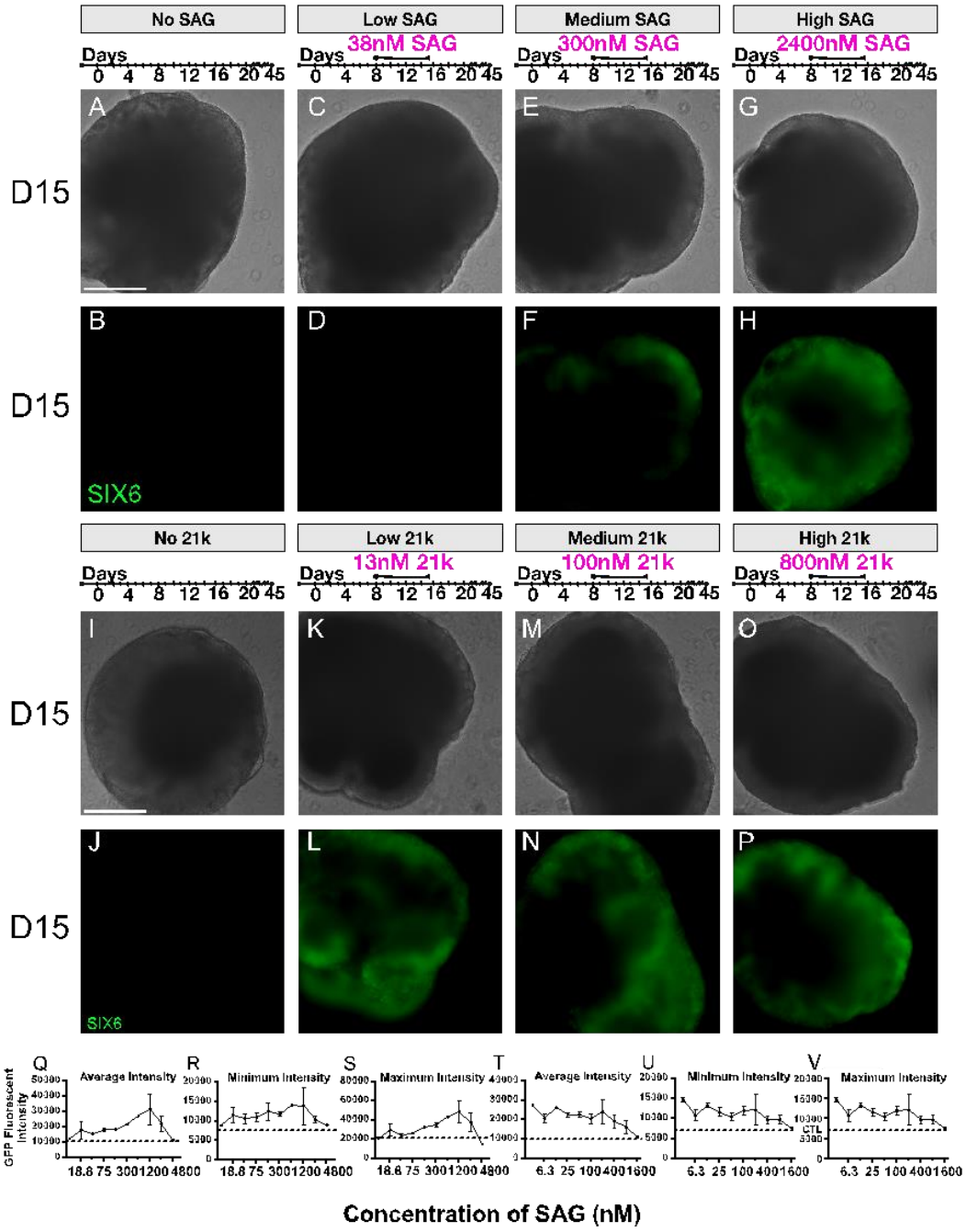

Figure 7. Optimization of SHH activator concentrations to promote SIX6-eGFP expression.

(**A-B**) Control untreated organoids from an IMR90.4 background with the SIX6-GFP reporter at 15 days. (**C-D**) Organoids treated with 38nM SAG from days 8-14; (**E-F**) 300nM SAG from days 8-14; (**G-H**) 2,400nM SAG from days 8-14; (**I-J**) untreated; (**K-L**) 13nM SAG21k from days 8-14; (**M-N**) 100nM SAG21K from days 8-14; and (**O-P**) 800nM SAG2k from days 8-14 all imaged at 15 days. (**Q-S**) Graphs depicting the (**Q**) average intensity (in arbitrary units), (**R**) minimum intensity (in arbitrary units), and (**S**) maximum intensity (in arbitrary units) of organoids treated with varying concentrations of SAG beginning at any day 8 and ending at 15 days. (**T-V**) A graph depicting the (**T**) average intensity (in arbitrary units), (**U**) minimum intensity (in arbitrary units), and (**V**) maximum intensity (in arbitrary units) of organoids treated with varying concentrations of SAG21k beginning at any day 8 and ending at 15 days. Dashed line represents untreated organoids. (**A-S**) scale bar represents 200µm. (**T-Y**) Error bars represent standard error of the mean. Graphs above panels depict the developmental protocol used to generate the images below.

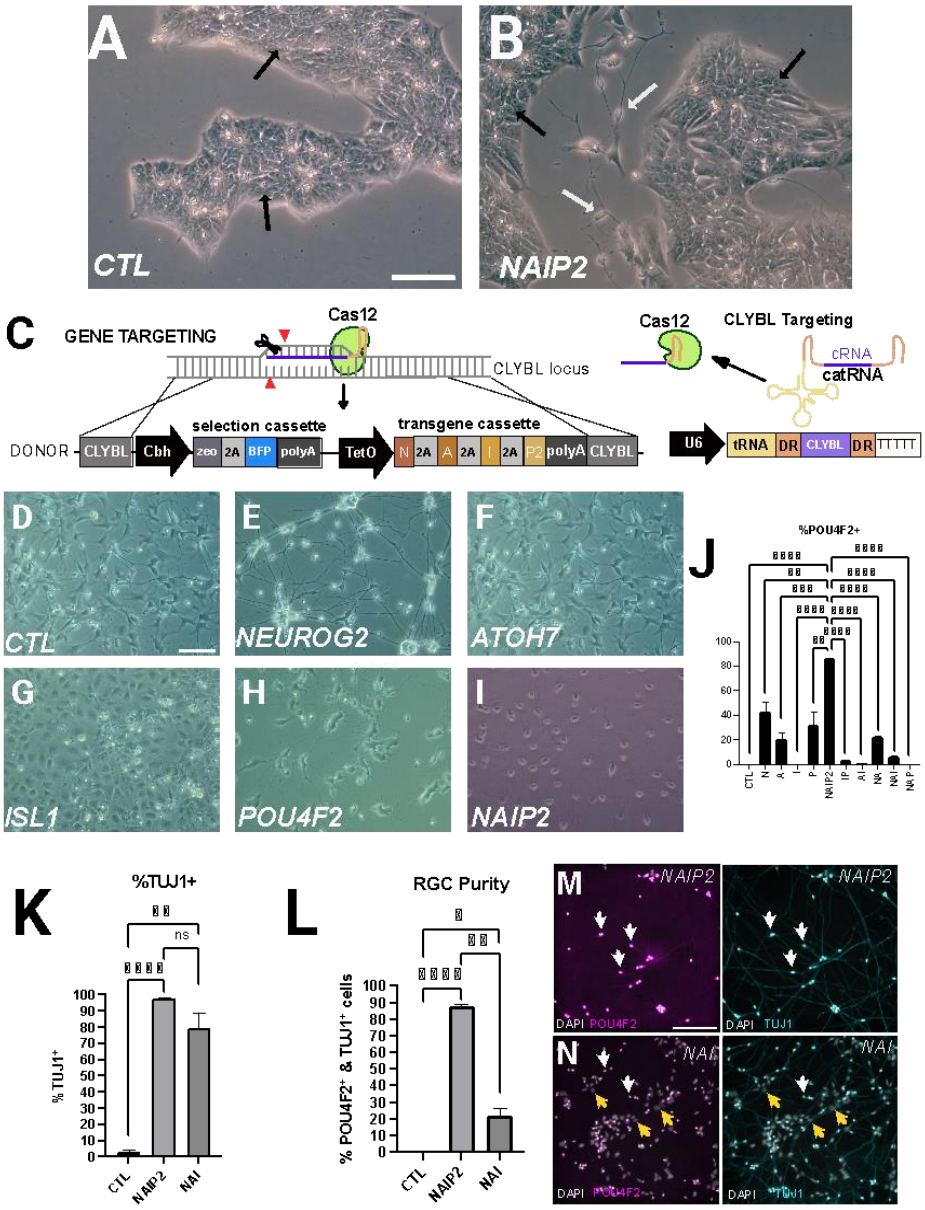

Figure 8. NAIP2 factor activation leads to the formation of RGC-like neurons.

Adapted from Agarwal et al., 2023. (**A**) Brightfield images of PSCs that were transiently transfected with a control (empty) plasmid and treated with dox for 3 days. (**B**) PSCs that were transiently transfected with NAIP2 plasmid and treated with dox for 3 days. (**C**) A schematic diagram depicting a U6 promoter-driven expression of an AsCas12a cRNA targeting the CLYBL safe harbor site for the insertion of a zeocin selectable (**D-I**) Tet-inducible transgene cassette with the NAIP2 cassette being depicted. Brightfield images of PSCs that have been dox treated and stably transfected with (**D**) empty cassette, © NEUROG2 cassette, (**F**) ATOH7 cassette, (**G**) ISLET1 cassette, (**H**) POU4F2 cassette, (**I**) and NAIP2 cassette. (**J**) Percent of POU4F2+ cells for each treatment group on day 6 relative to DAPI. (**K**) Percent of TUJ1+ neurons on day 6. (**L**) Percent of TUJ1+/POU4F2+ co-labelled RGC-iNs on day 6. (**M-N**) Image of POU4F2+ and TUJ1+ cells expressing (**M**) NAIP2 and (**N**) NAI taken at 6 days. Left depicts DAPI (white) and POU4F2 (magenta). Right depicts DAPI (white) and TUJ1 (cyan). (**A-B**): 100µm. Scale (**D-I**): 100µm. Scale (**M-N**): 100µm. For (**A-B**), black arrows label PSCs, while white arrows label converted neuron. For (M-N), white arrows label dual POU4F2+/TUJ1+ RGC-like neurons, yellow arrows label TUJ1+ and POU4F2- non-RGC neurons.

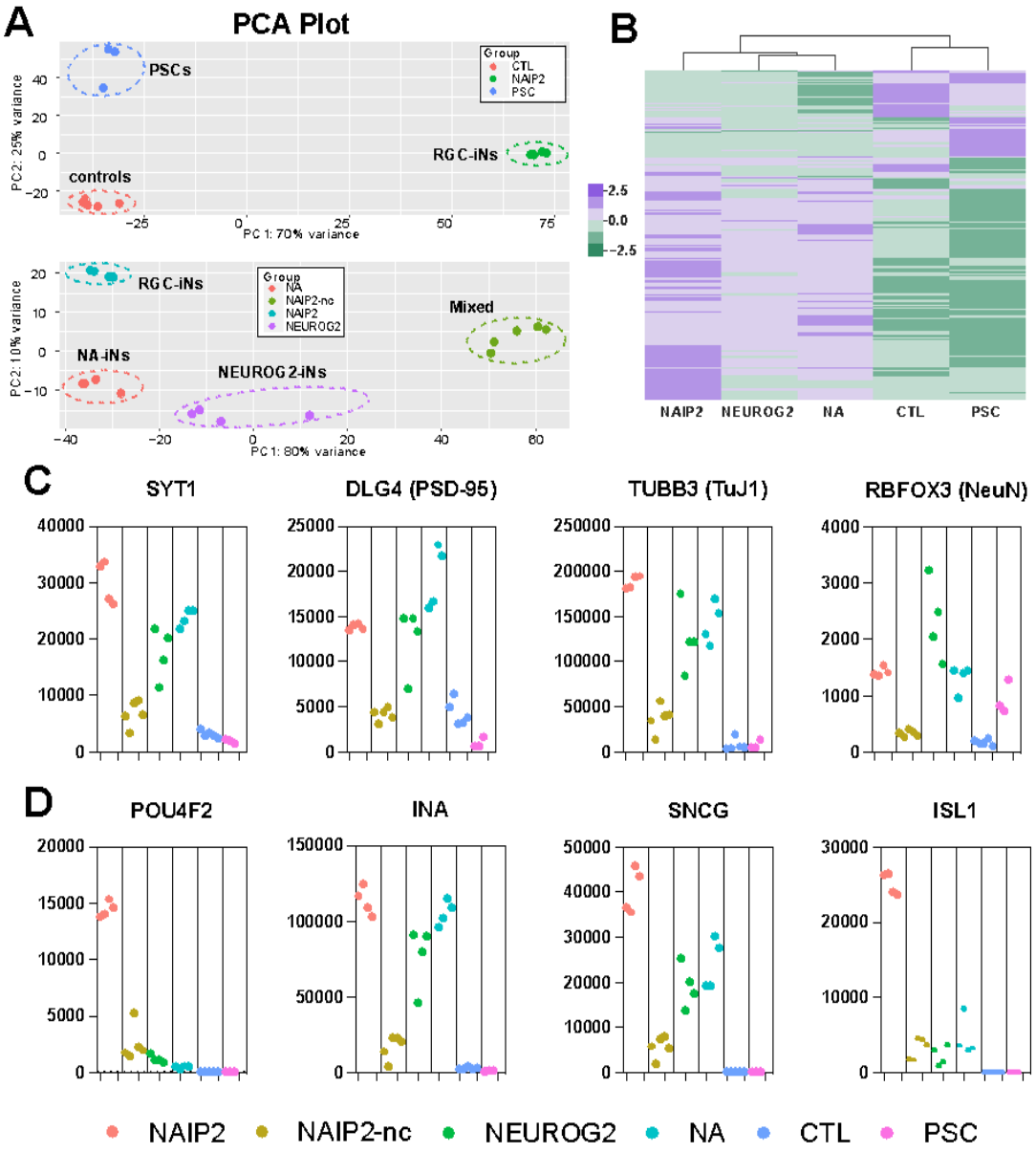

Figure 9. RGC-iNs express RGC-like transcriptomic profiles.

Adapted from Agarwal et al., 2023. (**A**) PCA plots comparing the expression profiles of each experimental condition. The top plot includes PSCs, empty cassette controls, and NAIP2 treated RGC-iNs. The bottom plot highlights the difference between RGC-iNs and other induced-neurons by including NAIP2 treated RGC-iNs, NA induced-neurons (NA-iNs), NEUROG2 induced-neurons (NEUROG2-iNs), and a mixed population generated by NAIP2 induced populations that have not been colony selected (Mixed). (**B**) A heatmap depicting the relative expression profiles of the top 500 most highly expressed genes found in RGC-iN across all experimental conditions. (**C-D**) Dot plots depict the expression profiles of (**C**) pan-neuronal markers and (**D**) RGC-specific markers across treatment groups. Peach dots represent treated NAIP2, yellow dots represent treated non-clonally selected NAIP2 cells, green dots represent treated NEUROG2, teal dots represent treated NEUROG2-ATOH7 treated cells, blue dots represent treated empty cassette cells, and pink dots represent PSCs.

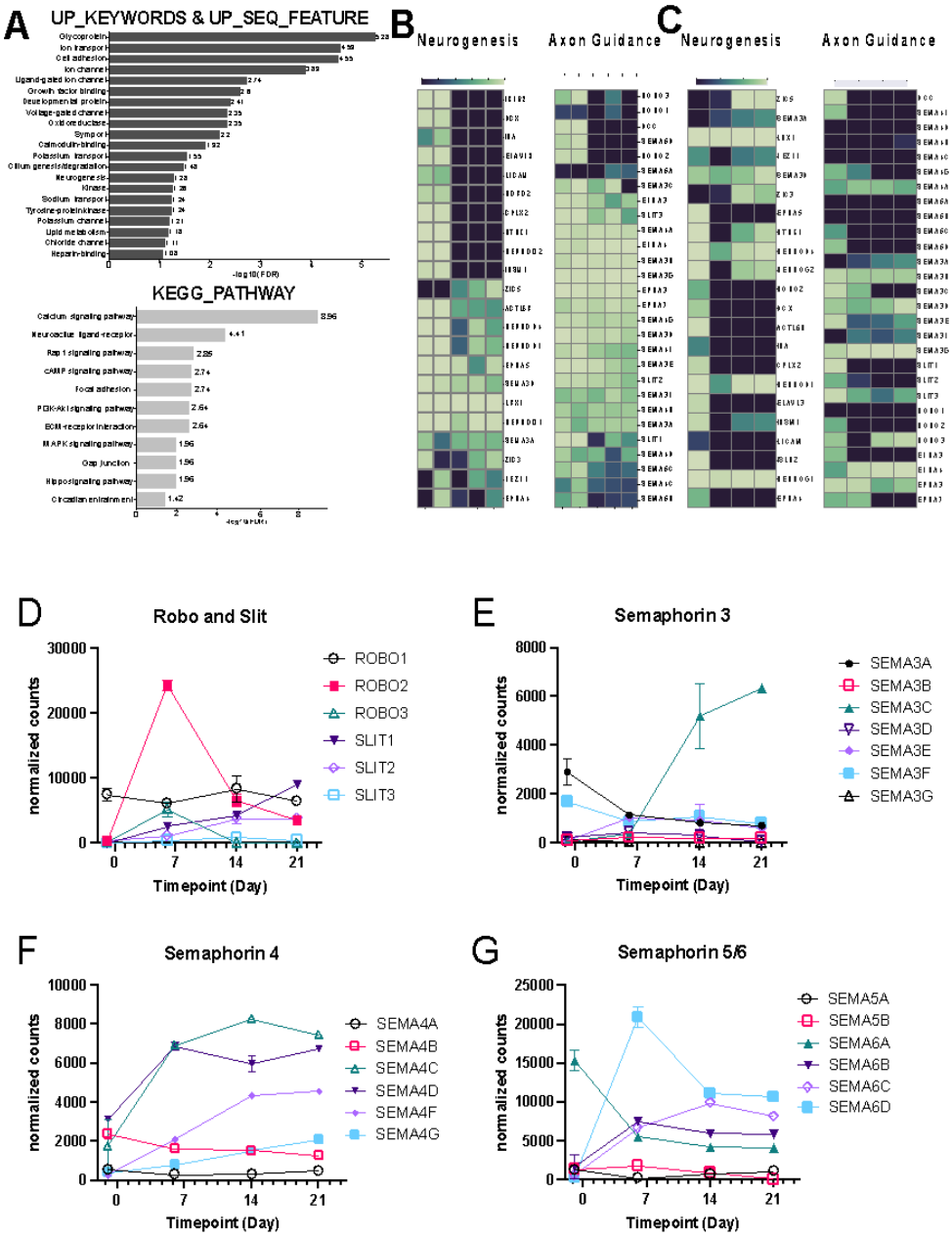

Figure 10. RGC-iNs have the potential to sense axon signaling cues.

Adapted from Agarwal et al., 2023 (**A**) A bar graph depicting the p-value of select pathways as identified by UniProt (UP) and Kyoto Encyclopedia of Genes and Genomes (KEGG) via the Database for Annotation, Visualization, and Integrated Discovery (DAVID). (**B**) Heatmaps of genes expressed within the neurogenesis (left) and axon guidance (right) pathways across different experimental conditions. (**C**) Heatmaps of genes expressed within the neurogenesis (left) and axon guidance (right) pathways from days 0 through 21. (**D-G**) Line graphs representing the expression profiles of (**D**) robo and slit, (**E**) class 3 semaphorins, (**F**) class 4 semaphorins, and (**G**) class 5 and 6 semaphorins in NAIP2 RGC-iNs sequenced at 0, 1, 2, and 3. Error bars represent SEM.

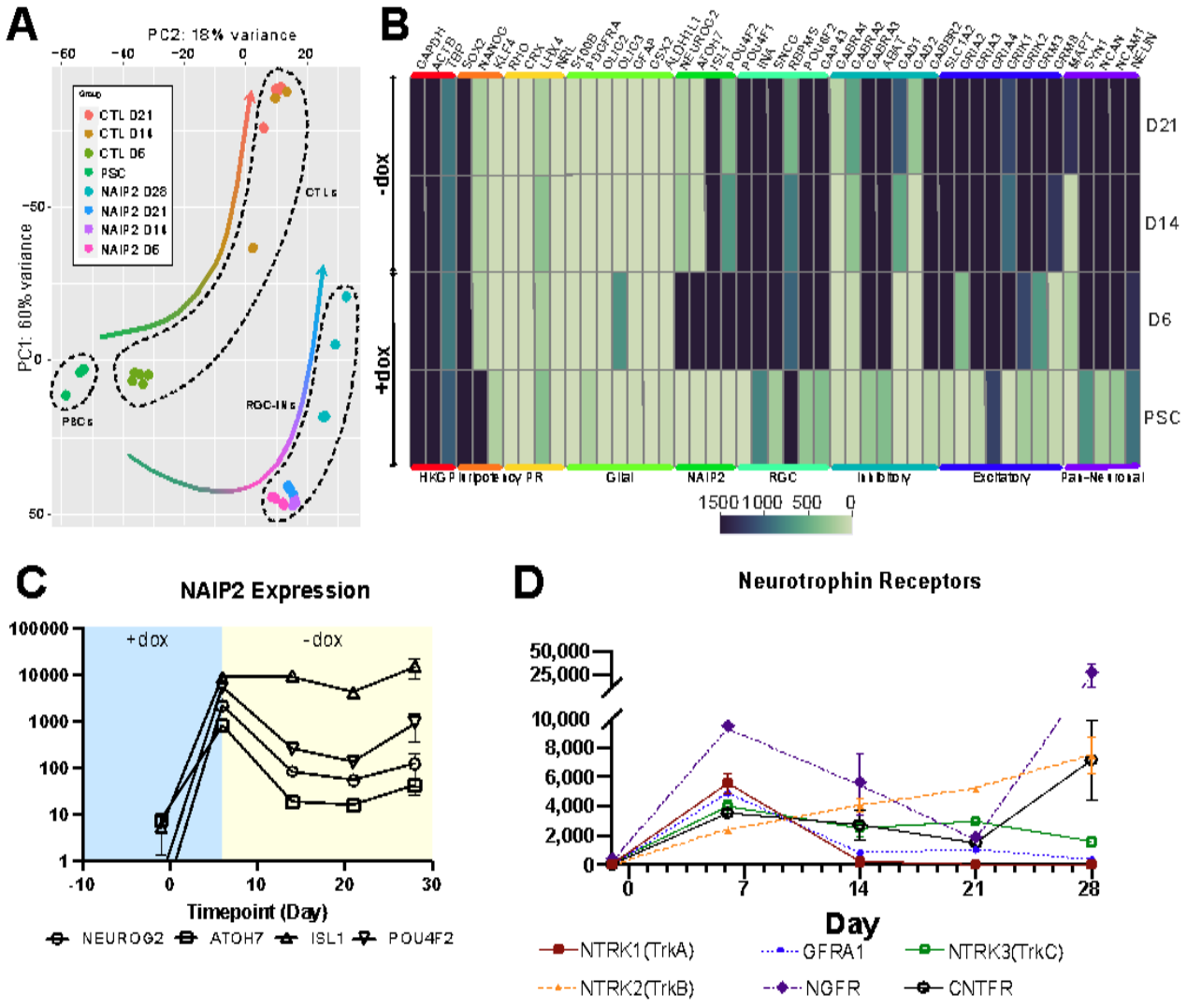

Figure 11. RGC-iNs exhibit temporal dynamics

Adapted from Agarwal et al., 2023 (**A**) A PCA plot depicting a diverging temporal trajectory of the RNAseq profiles of PSCs, empty cassette treated CTLs through 3 weeks, and NAIP2 treated RGC-iNs through 4 weeks. (**B**) Heatmap highlighting the expression of select cell type-specific markers in RGC-iNs through 3 weeks. (**C**) A line graph depicting the expression of the NAIP2 factors NEUROG2, ATOH7, ISL1, and POU4F2 through 4 weeks. (**D**) A line graph depicting the expression profile of neurotrophin receptors through four weeks.

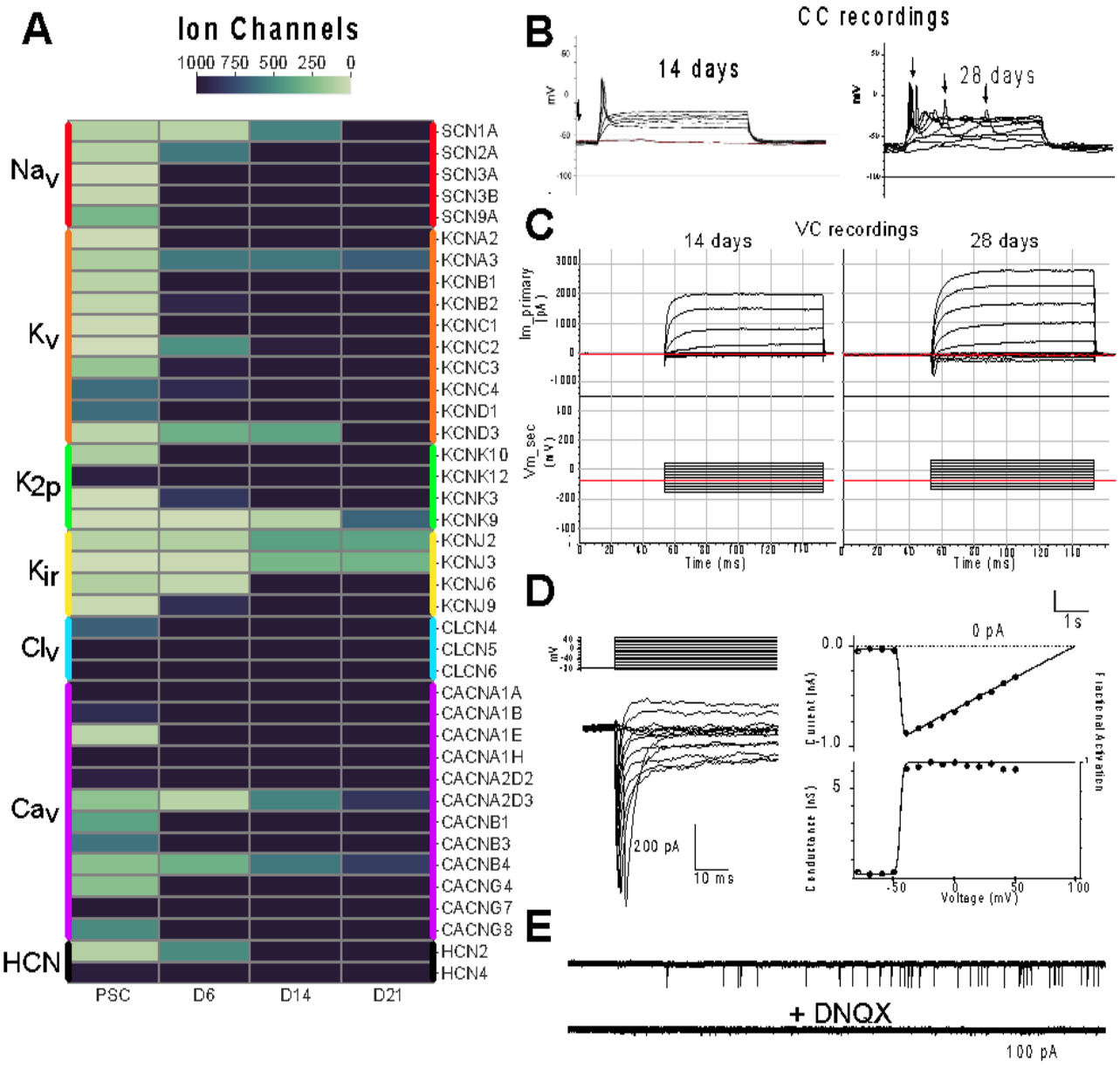

Figure 12. RGC-iNs are electrophysiologically active.

Adapted from Agarwal et al., 2023 (**A**) A heatmap depicting ion channel genes that are expressed at each timepoint. (**B**) Electrophysiological recordings from RGC-iNs under current clamp showing single action potentials elicited in response to depolarizing current injection as early as 14 days. By day 28, RGC-iNs are shown to exhibit repetitive action potentials. Resting membrane potential = −60 mV. Threshold current = 60 pA. (**C**) Under voltage clamp, depolarizing voltage steps in RGC-iNs reveal both fast inward Na+ and outward K+ currents, which are increased at day 28 compared to day 14. (**D**) (Left) An example AMPA puff (1 mM) evoked current in a voltage-clamped RGC-iN. (Right) I–V plot for AMPA puff evoked currents in RGC-iN (solid symbols), and linear fit (solid line). Traces on the left show time-course and double exponential fit to putative sEPSCs. (**E**) Example of current traces showing spontaneous excitatory post-synaptic currents (sEPSCs) that were blocked by the AMPA/Kainate antagonist DNQX.

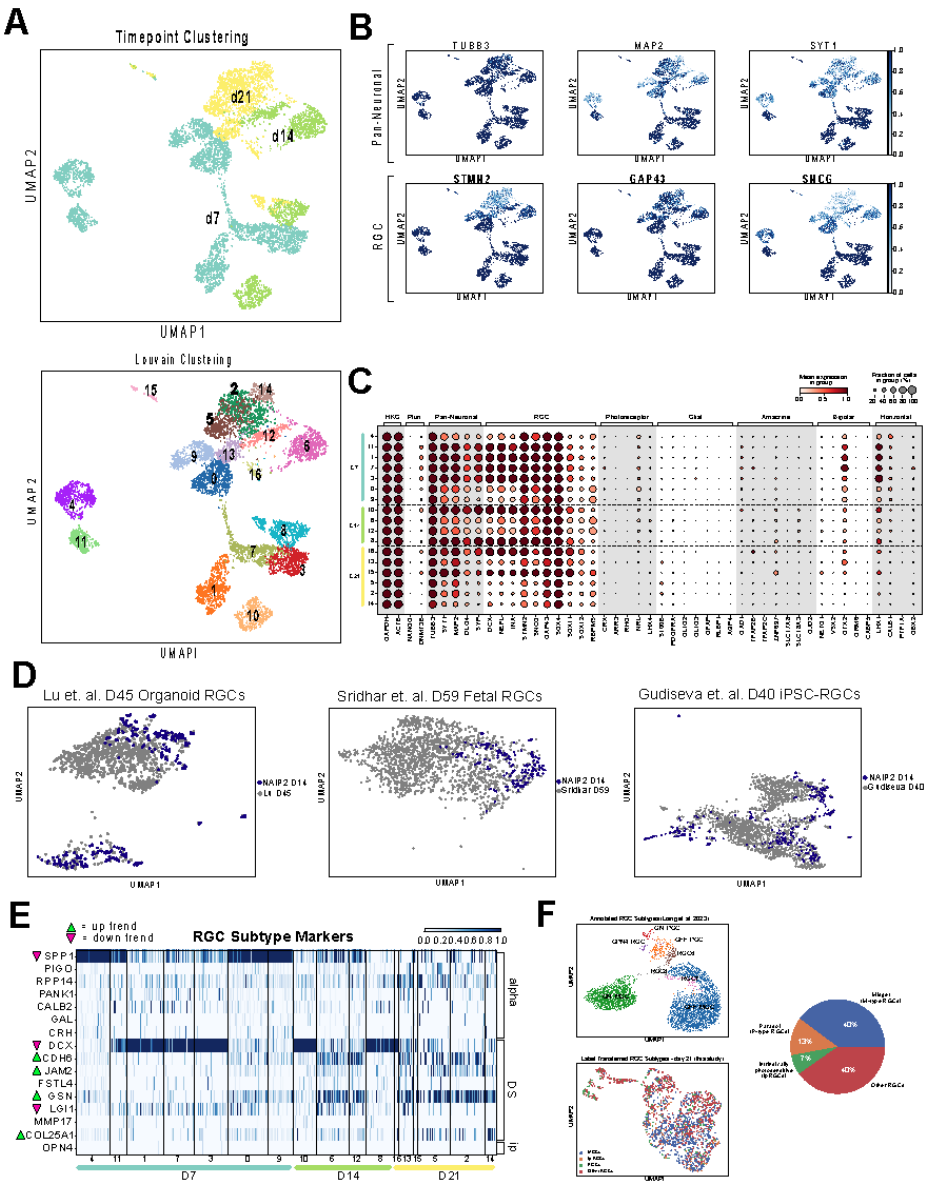

Figure 13. RGC-iNs scRNA-seq profiles are similar to those of fetal RGCs.

Adapted from Agarwal et al., 2023 (**A**) UMAPs of RGC-iNs colored by timepoint (top) and Louvain algorithm clustering (bottom). (**B**) UMAPs of RGC-iNs colored by the expression of select pan-neuronal markers (top) and RGC specific markers (bottom). (**C**) A dot plot showing the expression of various cell type marker genes in each cluster across 7, 14, and 21 day timepoints. Genes depicted include housekeeping genes (HKG), pluripotency markers (Pluri.), Pan-Neuronal markers, RGC markers, Photoreceptor markers, Glial markers, Amacrine markers, Bipolar markers, and Horizontal cell markers. (**D**) UMAPs highlighting the integration of NAIP2 day 14 RGC-iN clusters with published data from day 45 retinal organoid RGCs (left), day 59 fetal RGCs (center), and day 40 iPSC-RGCs (right). (**E**) A heatmap depicting normalized expression of various RGC-subtype specific markers in each RGC-iN cluster across 7, 14, and 21 days. Labels include those for alpha RGCs, directionally sensitive RGCs (DS), and intrinsically photosensitive RGCs (ip). (**F**) An annotated UMAP of subtype specific RGC-iNs taken from Liang et al., 2023 (top left). UMAP with RGC subtype labels transferred from Liang et al., 2023 onto day 21 RGC-iNs taken from this study (bottom left). A pie-chart depicting the RGC subtypes identified in day 21 RGC-iNs taken from this study (right).

REFERENCES

[1] H. Kolb, Simple Anatomy of the Retina. in: H. Kolb, E. Fernandez, and R. Nelson, (Eds.), Webvision: The Organization of the Retina and Visual System, Salt Lake City (UT), 1995.

[2] R.C. Hardie, and B. Minke, Calcium-dependent inactivation of light-sensitive channels in Drosophila photoreceptors. J Gen Physiol 103 (1994) 409-27.

[3] S. Nawy, Regulation of the on bipolar cell mGluR6 pathway by Ca2+. J Neurosci 20 (2000) 4471-9.

[4] F. Soto, J.C. Hsiang, R. Rajagopal, K. Piggott, G.J. Harocopos, S.M. Couch, P. Custer, J.L. Morgan, and D. Kerschensteiner, Efficient Coding by Midget and Parasol Ganglion Cells in the Human Retina. Neuron 107 (2020) 656-666 e5.

[5] Q. Liang, X. Cheng, J. Wang, L. Owen, A. Shakoor, J.L. Lillvis, C. Zhang, M. Farkas, I.K. Kim, Y. Li, M. DeAngelis, and R. Chen, A multi-omics atlas of the human retina at single-cell resolution. Cell Genom 3 (2023) 100298.

[6] A. Ferrena, X. Zhang, R. Shrestha, D. Zheng, and W. Liu, Six3 and Six6 jointly regulate the identities and developmental trajectories of multipotent retinal progenitor cells in the mouse retina. bioRxiv (2023).

[7] K.J. Wahlin, J. Cheng, S.L. Jurlina, M.K. Jones, N.R. Dash, A. Ogata, N. Kibria, S. Ray, K.C. Eldred, C. Kim, J.S. Heng, J. Phillips, R.J. Johnston, Jr., D.M. Gamm, C. Berlinicke, and D.J. Zack, CRISPR Generated SIX6 and POU4F2 Reporters Allow Identification of Brain and Optic Transcriptional Differences in Human PSC-Derived Organoids. Front Cell Dev Biol 9 (2021) 764725.

[8] J. Brodie-Kommit, B.S. Clark, Q. Shi, F. Shiau, D.W. Kim, J. Langel, C. Sheely, P.A. Ruzycki, M. Fries, A. Javed, M. Cayouette, T. Schmidt, T. Badea, T. Glaser, H. Zhao, J. Singer, S. Blackshaw, and S. Hattar, Atoh7-independent specification of retinal ganglion cell identity. Sci Adv 7 (2021).

[9] L.L. Molday, C.L. Cheng, and R.S. Molday, Cell-Specific Markers for the Identification of Retinal Cells and Subcellular Organelles by Immunofluorescence Microscopy. Methods Mol Biol 1834 (2019) 293-310.

[10] L.A. Remez, A. Onishi, Y. Menuchin-Lasowski, A. Biran, S. Blackshaw, K.J. Wahlin, D.J. Zack, and R. Ashery-Padan, Pax6 is essential for the generation of late-born retinal neurons and for inhibition of photoreceptor-fate during late stages of retinogenesis. Dev Biol 432 (2017) 140-150.

[11] C. Ozone, H. Suga, M. Eiraku, T. Kadoshima, S. Yonemura, N. Takata, Y. Oiso, T. Tsuji, and Y. Sasai, Functional anterior pituitary generated in self-organizing culture of human embryonic stem cells. Nat Commun 7 (2016) 10351.

[12] A.B. Simmons, S.J. Bloomsburg, S.A. Billingslea, M.M. Merrill, S. Li, M.W. Thomas, and P.G. Fuerst, Pou4f2 knock-in Cre mouse: A multifaceted genetic tool for vision researchers. Mol Vis 22 (2016) 705-17.

[13] J. Eintracht, M. Toms, and M. Moosajee, The Use of Induced Pluripotent Stem Cells as a Model for Developmental Eye Disorders. Front Cell Neurosci 14 (2020) 265.

[14] Y. Ishikawa, N. Yamamoto, M. Yoshimoto, and H. Ito, The primary brain vesicles revisited: are the three primary vesicles (forebrain/midbrain/hindbrain) universal in vertebrates? Brain Behav Evol 79 (2012) 75-83.

[15] J.M. Hebert, and G. Fishell, The genetics of early telencephalon patterning: some assembly required. Nat Rev Neurosci 9 (2008) 678-85.

[16] M.S. Byerly, and S. Blackshaw, Vertebrate retina and hypothalamus development. Wiley Interdiscip Rev Syst Biol Med 1 (2009) 380-389.

[17] K. Oishi, J. Chotiyanonta, D. Wu, M.I. Miller, S. Mori, K. Oishi, N. Pediatric Imaging, and S. Genetics, Developmental trajectories of the human embryologic brain regions. Neurosci Lett 708 (2019) 134342.

[18] F. Ulloa, and E. Marti, Wnt won the war: antagonistic role of Wnt over Shh controls dorso-ventral patterning of the vertebrate neural tube. Dev Dyn 239 (2010) 69-76.

[19] J.C. Sowden, J.K. Holt, M. Meins, H.K. Smith, and S.S. Bhattacharya, Expression of Drosophila omb-related T-box genes in the developing human and mouse neural retina. Invest Ophthalmol Vis Sci 42 (2001) 3095-102.

[20] S.H. Mui, J.W. Kim, G. Lemke, and S. Bertuzzi, Vax genes ventralize the embryonic eye. Genes Dev 19 (2005) 1249-59.

[21] M.J. Evans, and M.H. Kaufman, Establishment in culture of pluripotential cells from mouse embryos. Nature 292 (1981) 154-6.

[22] K. Takahashi, and S. Yamanaka, Induction of pluripotent stem cells from mouse embryonic and adult fibroblast cultures by defined factors. Cell 126 (2006) 663-76.

[23] J.S. Meyer, R.L. Shearer, E.E. Capowski, L.S. Wright, K.A. Wallace, E.L. McMillan, S.C. Zhang, and D.M. Gamm, Modeling early retinal development with human embryonic and induced pluripotent stem cells. Proc Natl Acad Sci U S A 106 (2009) 16698-703.

[24] T. Nakano, S. Ando, N. Takata, M. Kawada, K. Muguruma, K. Sekiguchi, K. Saito, S. Yonemura, M. Eiraku, and Y. Sasai, Self-formation of optic cups and storable stratified neural retina from human ESCs. Cell Stem Cell 10 (2012) 771-785.

[25] K.J. Wahlin, J.A. Maruotti, S.R. Sripathi, J. Ball, J.M. Angueyra, C. Kim, R. Grebe, W. Li, B.W. Jones, and D.J. Zack, Photoreceptor Outer Segment-like Structures in Long-Term 3D Retinas from Human Pluripotent Stem Cells. Sci Rep 7 (2017) 766.

[26] L. Wang, K. Meece, D.J. Williams, K.A. Lo, M. Zimmer, G. Heinrich, J. Martin Carli, C.A. Leduc, L. Sun, L.M. Zeltser, M. Freeby, R. Goland, S.H. Tsang, S.L. Wardlaw, D. Egli, and R.L. Leibel, Differentiation of hypothalamic-like neurons from human pluripotent stem cells. J Clin Invest 125 (2015) 796-808.

[27] W.K. Huang, S.Z.H. Wong, S.R. Pather, P.T.T. Nguyen, F. Zhang, D.Y. Zhang, Z. Zhang, L. Lu, W. Fang, L. Chen, A. Fernandes, Y. Su, H. Song, and G.L. Ming, Generation of hypothalamic arcuate organoids from human induced pluripotent stem cells. Cell Stem Cell 28 (2021) 1657-1670 e10.

[28] M.K. Jones, D. Agarwal, K.W. Mazo, M. Chopra, S.L. Jurlina, N. Dash, Q. Xu, A.R. Ogata, M. Chow, A.D. Hill, N.K. Kambli, G. Xu, R. Sasik, A. Birmingham, K.M. Fisch, R.N. Weinreb, R.A. Enke, D. Skowronska-Krawczyk, and K.J. Wahlin, Chromatin Accessibility and Transcriptional Differences in Human Stem Cell-Derived Early-Stage Retinal Organoids. Cells 11 (2022).

[29] D. Kim, J.M. Paggi, C. Park, C. Bennett, and S.L. Salzberg, Graph-based genome alignment and genotyping with HISAT2 and HISAT-genotype. Nat Biotechnol 37 (2019) 907-915.

[30] Y. Liao, G.K. Smyth, and W. Shi, featureCounts: an efficient general purpose program for assigning sequence reads to genomic features. Bioinformatics 30 (2014) 923-30.

[31] M.I. Love, W. Huber, and S. Anders, Moderated estimation of fold change and dispersion for RNA-seq data with DESeq2. Genome Biol 15 (2014) 550.

[32] S. Heinz, C. Benner, N. Spann, E. Bertolino, Y.C. Lin, P. Laslo, J.X. Cheng, C. Murre, H. Singh, and C.K. Glass, Simple combinations of lineage-determining transcription factors prime cis-regulatory elements required for macrophage and B cell identities. Mol Cell 38 (2010) 576-89.

[33] K. Miyama, G. Yamada, T.S. Yamamoto, C. Takagi, K. Miyado, M. Sakai, N. Ueno, and H. Shibuya, A BMP-inducible gene, dlx5, regulates osteoblast differentiation and mesoderm induction. Dev Biol 208 (1999) 123-33.

[34] B.T. Sherman, M. Hao, J. Qiu, X. Jiao, M.W. Baseler, H.C. Lane, T. Imamichi, and W. Chang, DAVID: a web server for functional enrichment analysis and functional annotation of gene lists (2021 update). Nucleic Acids Res 50 (2022) W216-W221.

[35] M. Kanehisa, and S. Goto, KEGG: kyoto encyclopedia of genes and genomes. Nucleic Acids Res 28 (2000) 27-30.

[36] M. Ashburner, C.A. Ball, J.A. Blake, D. Botstein, H. Butler, J.M. Cherry, A.P. Davis, K. Dolinski, S.S. Dwight, J.T. Eppig, M.A. Harris, D.P. Hill, L. Issel-Tarver, A. Kasarskis, S. Lewis, J.C. Matese, J.E. Richardson, M. Ringwald, G.M. Rubin, and G. Sherlock, Gene ontology: tool for the unification of biology. The Gene Ontology Consortium. Nat Genet 25 (2000) 25-9.

[37] C. Gene Ontology, S.A. Aleksander, J. Balhoff, S. Carbon, J.M. Cherry, H.J. Drabkin, D. Ebert, M. Feuermann, P. Gaudet, N.L. Harris, D.P. Hill, R. Lee, H. Mi, S. Moxon, C.J. Mungall, A. Muruganugan, T. Mushayahama, P.W. Sternberg, P.D. Thomas, K. Van Auken, J. Ramsey, D.A. Siegele, R.L. Chisholm, P. Fey, M.C. Aspromonte, M.V. Nugnes, F. Quaglia, S. Tosatto, M. Giglio, S. Nadendla, G. Antonazzo, H. Attrill, G. Dos Santos, S. Marygold, V. Strelets, C.J. Tabone, J. Thurmond, P. Zhou, S.H. Ahmed, P. Asanitthong, D. Luna Buitrago, M.N. Erdol, M.C. Gage, M. Ali Kadhum, K.Y.C. Li, M. Long, A. Michalak, A. Pesala, A. Pritazahra, S.C.C. Saverimuttu, R. Su, K.E. Thurlow, R.C. Lovering, C. Logie, S. Oliferenko, J. Blake, K. Christie, L. Corbani, M.E. Dolan, H.J. Drabkin, D.P. Hill, L. Ni, D. Sitnikov, C. Smith, A. Cuzick, J. Seager, L. Cooper, J. Elser, P. Jaiswal, P. Gupta, P. Jaiswal, S. Naithani, M. Lera-Ramirez, K. Rutherford, V. Wood, J.L. De Pons, M.R. Dwinell, G.T. Hayman, M.L. Kaldunski, A.E. Kwitek, S.J.F. Laulederkind, M.A. Tutaj, M. Vedi, S.J. Wang, P. D'Eustachio, L. Aimo, K. Axelsen, A. Bridge, N. Hyka-Nouspikel, A. Morgat, S.A. Aleksander, J.M. Cherry, S.R. Engel, K. Karra, S.R. Miyasato, R.S. Nash, M.S. Skrzypek, S. Weng, E.D. Wong, E. Bakker, T.Z. Berardini, L. Reiser, A. Auchincloss, K. Axelsen, G. Argoud-Puy, M. Blatter, E. Boutet, L. Breuza, A. Bridge, C. Casals-Casas, E. Coudert, A. Estreicher, M.L. Famiglietti, M. Feuermann, A. Gos, N. Gruaz-Gumowski, C. Hulo, N. Hyka-Nouspikel, F. Jungo, P. Le MMercier, D. Lieberherr, P. Masson, A. Morgat, I. Pedruzzi, L. Pourcel, S. Poux, C. Rivoire, S. Sundaram, A. Bateman, E. Bowler-Barnett, H. Bye-A-Jee, P. Denny, A/ Ignatchenko, R. Ishtiaq, A. Lock, Y. Lussi, M. Magrane, M. Martin, S. Orchard, P. Raposo, E. Speretta, N. Tyagi, K. Warner, R. Zaru, A. Diehl, R. Lee, J. Chan, S. Diamantakis, D. Raciti, M. Zarowiecki, M. Fisher, C. James-Zorn, V. Ponferrada, A. Zorn, S. Ramachandran, L. Ruzicka, M. Westerfield, The Gene Ontology knowledgebase in 2023. Genetics 224 (2023).

[38] C. UniProt, UniProt: the Universal Protein Knowledgebase in 2023. Nucleic Acids Res 51 (2023) D523-D531.

[39] W. Zhao, X. Ji, F. Zhang, L. Li, and L. Ma, Embryonic stem cell markers. Molecules 17 (2012) 6196-236.

[40] I. Decimo, F. Bifari, M. Krampera, and G. Fumagalli, Neural stem cell niches in health and diseases. Curr Pharm Des 18 (2012) 1755-83.

[41] F.M. Recchia, L. Xu, J.S. Penn, B. Boone, and P.J. Dexheimer, Identification of genes and pathways involved in retinal neovascularization by microarray analysis of two animal models of retinal angiogenesis. Invest Ophthalmol Vis Sci 51 (2010) 1098-105.

[42] K.D. Kaya, H.Y. Chen, M.J. Brooks, R.A. Kelley, H. Shimada, K. Nagashima, N. de Val, C.T. Drinnan, L. Gieser, K. Kruczek, S. Erceg, T. Li, D. Lukovic, Y.K. Adlakha, E. Welby, and A. Swaroop, Transcriptome-based molecular staging of human stem cell-derived retinal organoids uncovers accelerated photoreceptor differentiation by 9-cis retinal. Mol Vis 25 (2019) 663-678.

[43] D. Ortmann, and L. Vallier, Variability of human pluripotent stem cell lines. Curr Opin Genet Dev 46 (2017) 179-185.

[44] V. Chichagova, B. Dorgau, M. Felemban, M. Georgiou, L. Armstrong, and M. Lako, Differentiation of Retinal Organoids from Human Pluripotent Stem Cells. Curr Protoc Stem Cell Biol 50 (2019) e95.

[45] D. Hallam, G. Hilgen, B. Dorgau, L. Zhu, M. Yu, S. Bojic, P. Hewitt, M. Schmitt, M. Uteng, S. Kustermann, D. Steel, M. Nicholds, R. Thomas, A. Treumann, A. Porter, E. Sernagor, L. Armstrong, and M. Lako, Human-Induced Pluripotent Stem Cells Generate Light Responsive Retinal Organoids with Variable and Nutrient-Dependent Efficiency. Stem Cells 36 (2018) 1535-1551.

[46] D.P. Murphy, A.E. Hughes, K.A. Lawrence, C.A. Myers, and J.C. Corbo, Cis-regulatory basis of sister cell type divergence in the vertebrate retina. Elife 8 (2019).

[47] A.E. Hughes, J.M. Enright, C.A. Myers, S.Q. Shen, and J.C. Corbo, Cell Type-Specific Epigenomic Analysis Reveals a Uniquely Closed Chromatin Architecture in Mouse Rod Photoreceptors. Sci Rep 7 (2017) 43184.

[48] F. Memi, N. Zecevic, and N. Radonjic, Multiple roles of Sonic Hedgehog in the developing human cortex are suggested by its widespread distribution. Brain Struct Funct 223 (2018) 2361-2375.

[49] M. Kano, H. Suga, and H. Arima, Induction of Functional Hypothalamus and Pituitary Tissues From Pluripotent Stem Cells for Regenerative Medicine. J Endocr Soc 5 (2021) bvaa188.

[50] S. Douceau, T. Deutsch Guerrero, and J. Ferent, Establishing Hedgehog Gradients during Neural Development. Cells 12 (2023).

[51] C.M. Fligor, K.B. Langer, A. Sridhar, Y. Ren, P.K. Shields, M.C. Edler, S.K. Ohlemacher, V.M. Sluch, D.J. Zack, C. Zhang, D.M. Suter, and J.S. Meyer, Three-Dimensional Retinal Organoids Facilitate the Investigation of Retinal Ganglion Cell Development, Organization and Neurite Outgrowth from Human Pluripotent Stem Cells. Sci Rep 8 (2018) 14520.

[52] N. Tetreault, M.P. Champagne, and G. Bernier, The LIM homeobox transcription factor Lhx2 is required to specify the retina field and synergistically cooperates with Pax6 for Six6 trans-activation. Dev Biol 327 (2009) 541-50.

[53] Y. Ge, X. Chen, N. Nan, J. Bard, F. Wu, D. Yergeau, T. Liu, J. Wang, and X. Mu, Key transcription factors influence the epigenetic landscape to regulate retinal cell differentiation. Nucleic Acids Res 51 (2023) 2151-2176.

[54] V.M. Sluch, X. Chamling, M.M. Liu, C.A. Berlinicke, J. Cheng, K.L. Mitchell, D.S. Welsbie, and D.J. Zack, Enhanced Stem Cell Differentiation and Immunopurification of Genome Engineered Human Retinal Ganglion Cells. Stem Cells Transl Med 6 (2017) 1972-1986.

[55] T. Kuwajima, Y. Yoshida, N. Takegahara, T.J. Petros, A. Kumanogoh, T.M. Jessell, T. Sakurai, and C. Mason, Optic chiasm presentation of Semaphorin6D in the context of Plexin-A1 and Nr-CAM promotes retinal axon midline crossing. Neuron 74 (2012) 676-90.

[56] R.L. Matsuoka, K.T. Nguyen-Ba-Charvet, A. Parray, T.C. Badea, A. Chedotal, and A.L. Kolodkin, Transmembrane semaphorin signalling controls laminar stratification in the mammalian retina. Nature 470 (2011) 259-63.

[57] D. Wu, and W.M. Pardridge, Neuroprotection with noninvasive neurotrophin delivery to the brain. Proc Natl Acad Sci U S A 96 (1999) 254-9.

[58] C. Luscher, and R.C. Malenka, NMDA receptor-dependent long-term potentiation and long-term depression (LTP/LTD). Cold Spring Harb Perspect Biol 4 (2012).

[59] K.N. Paul, C. Fukuhara, M. Karom, G. Tosini, and H.E. Albers, AMPA/kainate receptor antagonist DNQX blocks the acute increase of Per2 mRNA levels in most but not all areas of the SCN. Brain Res Mol Brain Res 139 (2005) 129-36.

[60] I.C. Clark, K.M. Fontanez, R.H. Meltzer, Y. Xue, C. Hayford, A. May-Zhang, C. D'Amato, A. Osman, J.Q. Zhang, P. Hettige, J.S.A. Ishibashi, C.L. Delley, D.W. Weisgerber, J.M. Replogle, M. Jost, K.T. Phong, V.E. Kennedy, C.A.C. Peretz, E.A. Kim, S. Song, W. Karlon, J.S. Weissman, C.C. Smith, Z.J. Gartner, and A.R. Abate, Microfluidics-free single-cell genomics with templated emulsification. Nat Biotechnol 41 (2023) 1557-1566.

[61] Y. Lu, F. Shiau, W. Yi, S. Lu, Q. Wu, J.D. Pearson, A. Kallman, S. Zhong, T. Hoang, Z. Zuo, F. Zhao, M. Zhang, N. Tsai, Y. Zhuo, S. He, J. Zhang, G.L. Stein-O'Brien, T.D. Sherman, X. Duan, E.J. Fertig, L.A. Goff, D.J. Zack, J.T. Handa, T. Xue, R. Bremner, S. Blackshaw, X. Wang, and B.S. Clark, Single-Cell Analysis of Human Retina Identifies Evolutionarily Conserved and Species-Specific Mechanisms Controlling Development. Dev Cell 53 (2020) 473-491 e9.

[62] A. Sridhar, A. Hoshino, C.R. Finkbeiner, A. Chitsazan, L. Dai, A.K. Haugan, K.M. Eschenbacher, D.L. Jackson, C. Trapnell, O. Bermingham-McDonogh, I. Glass, and T.A. Reh, Single-Cell Transcriptomic Comparison of Human Fetal Retina, hPSC-Derived Retinal Organoids, and Long-Term Retinal Cultures. Cell Rep 30 (2020) 1644-1659 e4.

[63] H.V. Gudiseva, V. Vrathasha, J. He, D. Bungatavula, J.M. O'Brien, and V.R.M. Chavali, Single Cell Sequencing of Induced Pluripotent Stem Cell Derived Retinal Ganglion Cells (iPSC-RGC) Reveals Distinct Molecular Signatures and RGC Subtypes. Genes (Basel) 12 (2021).

[64] C. Xu, R. Lopez, E. Mehlman, J. Regier, M.I. Jordan, and N. Yosef, Probabilistic harmonization and annotation of single-cell transcriptomics data with deep generative models. Mol Syst Biol 17 (2021) e9620.

[65] R.L. Judson, J.E. Babiarz, M. Venere, and R. Blelloch, Embryonic stem cell-specific microRNAs promote induced pluripotency. Nat Biotechnol 27 (2009) 459-61.

[66] R. Nehme, E. Zuccaro, S.D. Ghosh, C. Li, J.L. Sherwood, O. Pietilainen, L.E. Barrett, F. Limone, K.A. Worringer, S. Kommineni, Y. Zang, D. Cacchiarelli, A. Meissner, R. Adolfsson, S. Haggarty, J. Madison, M. Muller, P. Arlotta, Z. Fu, G. Feng, and K. Eggan, Combining NGN2 Programming with Developmental Patterning Generates Human Excitatory Neurons with NMDAR-Mediated Synaptic Transmission. Cell Rep 23 (2018) 2509-2523.

[67] R.B. Hufnagel, T.T. Le, A.L. Riesenberg, and N.L. Brown, Neurog2 controls the leading edge of neurogenesis in the mammalian retina. Dev Biol 340 (2010) 490-503.

[68] F. Wu, T.J. Kaczynski, S. Sethuramanujam, R. Li, V. Jain, M. Slaughter, and X. Mu, Two transcription factors, Pou4f2 and Isl1, are sufficient to specify the retinal ganglion cell fate. Proc Natl Acad Sci U S A 112 (2015) E1559-68.

[69] X.M. Zhang, T. Hashimoto, R. Tang, and X.J. Yang, Elevated expression of human bHLH factor ATOH7 accelerates cell cycle progression of progenitors and enhances production of avian retinal ganglion cells. Sci Rep 8 (2018) 6823.

[70] S.K. Ohlemacher, A. Sridhar, Y. Xiao, A.E. Hochstetler, M. Sarfarazi, T.R. Cummins, and J.S. Meyer, Stepwise Differentiation of Retinal Ganglion Cells from Human Pluripotent Stem Cells Enables Analysis of Glaucomatous Neurodegeneration. Stem Cells 34 (2016) 1553-62.

[71] S.L. Ji, and S.B. Tang, Differentiation of retinal ganglion cells from induced pluripotent stem cells: a review. Int J Ophthalmol 12 (2019) 152-160.

[72] J.R. Sanes, and R.H. Masland, The types of retinal ganglion cells: current status and implications for neuronal classification. Annu Rev Neurosci 38 (2015) 221-46.

[73] W. Yan, Y.R. Peng, T. van Zyl, A. Regev, K. Shekhar, D. Juric, and J.R. Sanes, Cell Atlas of The Human Fovea and Peripheral Retina. Sci Rep 10 (2020) 9802.

[74] J.L. Whyte, A.A. Smith, and J.A. Helms, Wnt signaling and injury repair. Cold Spring Harb Perspect Biol 4 (2012) a008078.

[75] Y. Peng, J. Li, H. Lin, S. Tian, S. Liu, F. Pu, L. Zhao, K. Ma, X. Qing, and Z. Shao, Endogenous repair theory enriches construction strategies for orthopaedic biomaterials: a narrative review. Biomater Transl 2 (2021) 343-360.

[76] J. Lyu, and X. Mu, Genetic control of retinal ganglion cell genesis. Cell Mol Life Sci 78 (2021) 4417-4433.

[77] G.B. Carballo, J.R. Honorato, G.P.F. de Lopes, and T. Spohr, A highlight on Sonic hedgehog pathway. Cell Commun Signal 16 (2018) 11.

[78] M.E. Ritchie, B. Phipson, D. Wu, Y. Hu, C.W. Law, W. Shi, and G.K. Smyth, limma powers differential expression analyses for RNA-sequencing and microarray studies. Nucleic Acids Res 43 (2015) e47.

[79] J.T. Robinson, H. Thorvaldsdottir, W. Winckler, M. Guttman, E.S. Lander, G. Getz, and J.P. Mesirov, Integrative genomics viewer. Nat Biotechnol 29 (2011) 24-6.

[80] T. Liu, J.A. Ortiz, L. Taing, C.A. Meyer, B. Lee, Y. Zhang, H. Shin, S.S. Wong, J. Ma, Y. Lei, U.J. Pape, M. Poidinger, Y. Chen, K. Yeung, M. Brown, Y. Turpaz, and X.S. Liu, Cistrome: an integrative platform for transcriptional regulation studies. Genome Biol 12 (2011) R83.

[81] W. Huang da, B.T. Sherman, and R.A. Lempicki, Systematic and integrative analysis of large gene lists using DAVID bioinformatics resources. Nat Protoc 4 (2009) 44-57.